VAP-mediated membrane tethering mechanisms implicate ER-PM contact function in pH homeostasis

Kar Ling Hoh [1, 2, 3], Baicong Mu [1, 2, 3], Tingyi See [1, 3], Amanda Yunn Ee Ng [1, 2], Annabel Qi En Ng [1], and Dan Zhang [1, 2, *]

[1]Temasek Life Sciences Laboratory, 1 Research Link, National University of Singapore, 117604, Singapore; [2]Department of Biological Sciences, National University of Singapore, 14 Science Drive 4, Singapore 117543, Singapore.

[3]These authors contributed equally to this work

[*]Address correspondence to Dan Zhang (zhangdan@tll.org.sg)

Abstract

VAMP-associated proteins (VAPs) are highly conserved endoplasmic reticulum (ER) resident proteins that establish ER contacts with multiple membrane compartments in many eukaryotes. However, VAP-mediated membrane tethering mechanisms remain ambiguous. Here, focusing on fission yeast ER-plasma membrane (PM) contact formation, using systematic interactome analyses and quantitative microscopy, we predict a non-protein-protein binding-based tethering mechanism of VAPs. We further demonstrate that VAP-anionic phospholipids interactions underlie ER-PM association and define the pH-responsive nature of VAP-tethered membrane contacts. Importantly, such conserved interactions, particularly with phosphatidylinositol 4-phosphate (PI_4P) and phosphatidylinositol (PI), are defective in amyotrophic lateral sclerosis (ALS)-associated human VAPB mutant. Moreover, we identify a conserved FFAT-like motif locating at the autoinhibitory hotspot of the essential PM proton pump Pma1. This modulatory VAP-Pma1 interaction is crucial for pH homeostasis. We thus propose an ingenious strategy for maintaining intracellular pH by coupling Pma1 modulation with pH-biosensory ER-PM contacts via VAP-mediated interactions.

Introduction

In eukaryotes, membrane-bound organelles with characteristic morphologies, dynamics, and functions, are interconnected at membrane contact sites (MCSs) where respective activities can be jointly regulated. A number of conserved tethering proteins has been identified at different MCSs [1,2]. Among them, VAPs (Scs2 and Scs22 in yeasts; VAPA and VAPB in human) are the only ER resident anchors connecting various proteins at multiple MCSs via FFAT (two phenylalanines/F in an acidic tract) or its related motifs. Each VAP contains an N-terminal conserved major sperm protein (MSP) domain bathing in the cytosol and a

transmembrane segment at the extreme C-terminus [3,4]. In both budding and fission yeasts, VAPs are the major tethers for ER-PM association [5,6]. Unlike other yeast ER-PM tethering proteins, namely tricalbins (Tcb1/2/3) and Ist2 which directly bind acidic phospholipids (PLs) in the PM [7,8], molecular basis for VAP-mediated ER-PM contact formation is however still unknown.

VAP-mediated ER-PM contacts have been functionally linked to lipid homeostasis in yeast. VAPs recruit OSBP-related protein (ORP)/oxysterol-binding homology (Osh) family via FFAT-binding to ER-PM junctions and regulate their PI_4P/sterol transferring activities to keep PI_4P level in the PM [9]. Other roles of ER-PM contacts in ER organization and stress signaling have also been suggested [6]. Moreover, tight ER-PM junctions can impose steric effects on cortical events. Such physical roles have been mainly established for contractile ring assembly and for delimiting exocytic territory in the fission yeast *Schizosaccharomyces pombe* (*S. pombe*) [10-12]. Here, for the first time, we expand VAP-mediated ER-PM contact functions to pH homeostasis using *S. pombe.*

In the PM of fungi and plant cells, proton pumping P-type adenosine triphosphatases (ATPase) (known as Pma1 in yeast) maintain the intracellular pH and membrane potential essential for nutrient uptake [13]. Pma1 assembles as hexamers [14]. Each monomer contains multiple transmembrane α-helices (TMs) and four major cytosolic domains: the actuator (A) domain, the nucleotide-binding (N) domain, the phosphorylation (P) domain, and the C-terminal regulatory (R) domain which is autoinhibitory by locking other cytosolic domains via intra- or inter-molecular interactions [15,16]. Glucose-dependent phosphorylation of R domain has been postulated to activate these pumps in yeast by abolishing such interactions [17]. However, it is unknown if other glucose-independent mechanisms have been evolved for Pma1 regulation.

In this study, we demonstrated that VAPs establish pH-sensitive ER-PM contacts through electrostatic interactions with major PM anionic PLs, especially high-abundance PI and phosphatidylserine (PS). Our finding thus recognizes the MSP as a conserved lipid-binding domain and unifies that lipid-protein interactions dominate ER-PM contact formation. Our interactome analyses also revealed major VAP interactors and implicated potential roles of VAPs in various cellular events. Importantly, we pinpointed a conserved FFAT-like motif in Pma1 at its autoinhibitory P-R domain binding site and confirmed that such VAP interaction is protective against cytoplasmic acidification and crucial for pH homeostasis. We therefore propose that VAPs sustain cytosolic pH by finetuning their interactions between Pma1 and pH-sensory PLs at ER-PM contacts.

Results

Fission yeast VAPs establish ER-PM contacts via the conserved MSP domain in a dosage-dependent manner

A previous study has shown that Scs2 plays a dominant role in ER-PM tethering over Scs22 in fission yeast [5] (see also Fig. 1a). In fact, Scs2 was expressed at a much higher level than Scs22 in wild type (*WT*) (Fig. 1b). Interestingly, ER-PM contact formation was also compromised when we swapped the open reading frames of *scs2* and *scs22* at their genomic loci (Supplementary Fig. 1a), implying that there might be intrinsic differences between two VAPs in their ER-PM tethering function.

Unlike Scs22 where its nuclear envelope (NE) localization was obvious, the NE pool of Scs2 was barely visible, suggesting likely stronger affinity of Scs2 towards the cell cortex (Fig. 1c). We then ectopically expressed Scs2 or Scs22 at various levels in cells lacking native VAPs (Fig. 1b). We chose the promoter of *pil1* that encodes an abundant eisosome subcomponent [18] to achieve high protein expression. Scs2 always exhibited higher cortex-to-

NE ratios than Scs22 under similar expression levels. Moreover, despite both VAPs could dose-dependently restore ER-PM contacts in *scs2Δscs22Δ* cells, Scs2 appeared more competent in ER-PM tethering (Fig. 1c). We envisaged that strong PM binding of an ER-PM tether might dampen its mobility. In line with this, the artificial tether TM-GFP-CSS_{Ist2} which resides in the ER and binds to the PM [5] displayed a slower fluorescence recovery after photobleaching (FRAP) along the cell cortex than the control ER-resident TM-GFP (Supplementary Fig. 1b). Similarly, Scs2 always diffused slower than Scs22 in *WT* or in *scs2Δscs22Δ* cells when expressed in comparable levels (Supplementary Fig. 1c). We thus conclude that Scs2 harbors an intrinsic higher PM affinity than Scs22.

Notably, mutations of three lysine residues (K36/38/43A, hereafter referred to as 3KA) in the VAP consensus sequence (VCS) within the MSP domain [19] of either Scs2 or Scs22 abolished their ER-PM tethering capacity regardless of high expression levels (Fig. 1b-d). As expected, both $Scs2^{3KA}$ and $Scs22^{3KA}$ nearly lost the PM affinity, manifested by either reduced cortex-to-NE ratios or increased mobility to levels of non-tether ER proteins (i.e., the ER luminal marker mCherry-ADEL [20] for cortex-to-NE ratios and TM-GFP for mobility in Fig. 1c and Supplementary Fig. 1c). These data indicate that the PM affinity of a VAP is likely determined by its conserved MSP domain. We then constructed chimeric variants by swopping MSP domains between Scs2 and Scs22 (Fig. 1d) and expressed them in *scs2Δscs22Δ* cells at comparable levels (Supplementary Fig. 1d). Indeed, MSP_{Scs2}-containing constructs always exhibited higher cortex-to-NE ratios than the ones with MSP_{Scs22} (Fig. 1e).

Collectively, our results suggest that the conserved MSP domain intrinsically defines dose-dependent ER-PM tethering capacity of VAPs.

Fission yeast VAPs maintain the PM PI_4P level via the conserved MSP domain in a dosage-dependent manner

It has been shown that fission yeast cells lacking both VAPs display elevated PM PI_4P levels marked by the pleckstrin homology (PH) domain of budding yeast Osh2 [5] (see also Supplementary Fig. 1e). Such abnormally high PI_4P levels of the PM cannot be rescued by artificially re-built ER-PM contacts [5], indicating specific roles of VAPs in the PM PI_4P homeostasis.

As compared to *WT*, we found that levels of the PM PI_4P remained high in *scs2Δscs22Δ* expressing low levels of either VAPs where ER-PM contact re-establishment was incomplete (Supplementary Fig. 1f). Intriguingly, unlike wild-type VAPs or even chimeric variants that still contained intact MSP domains, high expression of either $Scs2^{3KA}$ or $Scs22^{3KA}$ in *scs2Δscs22Δ* failed to reduce the high PM level of PI_4P (Supplementary Fig. 1f). These data suggest the necessity of a functional MSP domain for PI_4P-related activity of VAPs. Therefore, we conclude that roles of VAPs in the PM PI_4P homeostasis require the MSP domain in a dose-dependent manner.

Interactome analyses reveal divergent binding preferences between two VAPs

We next attempted to explore molecular interactions underlying VAP-mediated membrane tethering. Given that Scs2 and Scs22 showed distinct PM affinities, we speculated that they may also differ in their potential cortical binding partners. We performed interactome analyses using both full-length and TM-truncated VAPs (namely Scs2N and Scs22N) as baits.

Interestingly, many interactors shared by all four baits were lipid enzymes or lipid transporters (Fig. 2a and Supplementary Data 1). Interactors involved in cell polarity or morphogenesis that are localized to cell tips showed an overall binding preference to Scs2 and Scs2N (Supplementary Fig. 2a). This may partly explain the fact that Scs22 was less capable of establishing ER-PM contacts at cell ends (arrowed in Fig. 1c). Proteins that

organize the lateral cell cortex were also detected to preferentially bind Scs2 (Supplementary Fig. 2a). Notably, 49 out of total 296 interactors detected with at least one bait were related to vesicle-mediated trafficking. Among these major hits, regulatory proteins mainly associated with Scs22, while coatomers and SNARE/NSF-related factors appeared to favor Scs2 binding (Supplementary Fig. 2a). We then picked the top five Scs2-favored interactors which localized to the lateral PM and verified such interactions using Co-immunoprecipitation (Co-IP) (Fig. 2b and Supplementary Fig. 2b) [21]. We also confirmed Scs2-Scs22 interaction by Co-IP (Fig. S2c).

Many VAP-interacting proteins contain the FFAT motif which has been shown to bind the MSP domain via electrostatic interactions [22]. A position weight matrix has been established for calculating a FFAT score of any given 13-residue motif that predicts its VAP binding potential (FFAT score of an ideal motif is 0 and 2.5 is the typical cutoff score) [4,23]. Remarkably, most interactors we detected or confirmed did not contain a typical FFAT motif (Fig. 2b, Supplementary Fig. 2a-d and Supplementary Data 1). We also did not detect peptide-enrichment of proteins with low FFAT scores (Supplementary Fig. 2d), implying a possible existence of more complex interaction patterns for fission yeast VAPs beyond FFAT-based association.

In summary, we revealed that Scs2 and Scs22 differed in protein binding preference, especially with cortical proteins.

Interactome analyses implicate VAPs in possible modulation of Sec14 family functions

We noticed that four out of five Sec14-like lipid transporters were detected in Scs2 interactome (Fig. 2c), with previously uncharacterized Csr102 and Pdr16 as top two hits (Fig. 2b). Sec14 family proteins have been suggested to engage in PI transfer, however importance of such lipid-related function *in vivo* is still obscure for both fission and budding yeasts [24,25].

We found that both the PM and Golgi pools of PI_4P decreased significantly in tubby-shaped *sec14Δ* cells. Such reduction was enhanced when cells further lost either or both of Csr102 and Pdr16 in the background, whereas mutants with single or double deletion of *csr102* and *pdr16* remained *WT*-like (Fig. 2d). No detectable change of phosphatidylinositol 4,5-bisphosphate ($PI_{4,5}P_2$) levels was seen in all these mutants (data not shown). Our data suggest that Sec14 family proteins contribute to PI_4P homeostasis in *S. pombe*.

Interestingly, Csr102 bound both VAPs at their respective native levels, and exhibited a likely higher affinity to Scs22 when VAPs were ectopically expressed in a comparable level in *scs2Δscs22Δ* background (Fig. 2b and Supplementary Fig. 2e). Such interactions were required for its cortical localization, as Csr102 became cytosolic in absence of both VAPs even when ER-PM contacts were artificially restored (Fig. 2e and Supplementary Fig. 2f). Indeed, both $Scs2^{3KA}$ and $Scs22^{3KA}$ that mostly lost Csr102-interaction failed to recruit Csr102 to the cortex (Supplementary Fig. 2e and Fig. 2f). In contrast, the cortical localization of Pdr16 was VAP-independent (Supplementary Fig. 2g). Except Scs2, Pdr16 did not interact with $Scs2^{3KA}$, Scs22 or $Scs22^{3KA}$, even when these VAP variants were highly expressed (Supplementary Fig. 2h and Fig. 2b). Though it is unclear how VAP-interactions would affect Sec14 family activities in PI_4P homeostasis, it is attractive to speculate such a modulatory role of VAPs at least via Csr102.

A prediction of non-protein-protein interaction-based ER-PM tethering mechanism for VAPs

We think that cross-membrane interactions are the basis of establishing MCSs of any kind, including VAP-mediated ER-PM tethering. Dosage-dependent ER-PM tethering of VAPs we hitherto demonstrated somewhat implies the existence of collectively abundant PM

interaction partners which could afford unsaturated interactions with VAPs of high expression levels.

To further explore molecular basis of VAP-mediated ER-PM tethering, we focused on the top five Scs2-interactors localizing to the lateral PM (Fig. 2b and Supplementary Fig. 2b). Among them, Myo1 appears least likely a key tethering partner, as it is dynamically associated with endocytic sites and mainly enriched at growing tips with a limited pool along the interphase lateral cell cortex [26]. To the contrary, Pil1 and the essential H+-ATPase Pma1 are known highly abundant and static landmarks laterally covering distinct PM domains [18,27] (Supplementary Fig. 2i). However, no reduction of ER-PM contacts was seen in *csr102Δpdr16Δpil1Δ* cells, and Scs2 could still establish ER-PM contacts at cortical regions devoid of Pma1 in the background (Fig. 2g). Besides, Scs2 diffused much faster than these PM interactors (Supplementary Fig. 2i), but at similar rates as the artificial ER-PM tether (Supplementary Fig. 1b,c) that binds anionic PLs of the PM [5,28]. These results suggest the presence of other major cortical partners and a likelihood of non-protein-protein interaction-based tethering for VAPs.

In fact, we detected rather limited number of ER resident interactors using cytosolic Scs2N (Supplementary Data 1). We reason that if PM proteins were indeed required for Scs2-mediated ER-PM contact formation, PM-anchored Scs2 would be otherwise an incompetent tether. We thus constructed PM-anchored Scs2 (hereafter referred as Scs2-PM) by replacing its C-terminal TM domain with a PM targeting motif [29] and ectopically expressed it under the strong thiamine (Thi)-repressible *nmt1* or *pi11* promoter in *scs2Δscs22Δ* cells. Fascinatingly, though not as fully efficient as *WT*, Scs2-PM was able to establish ER-PM contacts in a dose-dependent manner, which similarly required a functional MSP domain (Fig. 3a). Surprisingly, like *WT* (Supplementary Fig. 1f), Scs2-PM was able to restore the PM PI_4P level in *scs2Δscs22Δ* cells, while $Scs2^{3KA}$-PM again lost the competence (Fig. 3b). Likewise, the

cortical recruitment of Csr102 was fully rescued by Scs2-PM, but not Scs2^{3KA}-PM (Supplementary Fig. 3a).

Taken together, our data predict that protein-protein interactions are likely dispensable for Scs2-mediated ER-PM association.

VAPs interact with major anionic phospholipids

We next sought to explore possible PLs-interaction of VAPs and envisaged that such potential PLs should be abundant in both the PM and the ER, for instance, main anionic PLs - PI and PS [30,31].

In fact, purified Scs2N-6His could bind both PI and PS liposomes. Such binding was enhanced with increased PI or PS concentration, or by adding PI_4P to respective liposomes (Supplementary Fig. 3b). Unfortunately, recombinant Scs2N^{3KA}-6His was unsuitable for liposome co-sedimentation assays as it generally precipitated after centrifugation (data not shown). We thus developed a quantitative fluorescence microscopy-based protein-liposome binding assay (see Methods). In brief, we examined protein-liposome binding using rhodamine-labelled liposomes with magnetic beads that were immuno-conjugated with GFP-tagged cytosolic portions of VAP variants. Concordantly, Scs2N showed specific binding to PI and PS, while Scs2N^{3KA} clearly exhibited much lower affinities to both (Fig. 3c and Supplementary Fig. 3c). Likewise, addition of either PI_4P or $PI_{4,5}P_2$ to PI liposomes increased Scs2N binding affinity, and such effects were slightly more pronounced with PI_4P (Supplementary Fig. 3d). Remarkably, Scs22N also could bind to PI and PS, but exhibiting generally weaker binding as compared to Scs2N. Unlike Scs2N^{3KA}, Scs22N^{3KA} fully lost binding to PI or PS (Fig. 3d). Notably, such PLs-interaction patterns of fission yeast VAPs and their mutants were well correlated with their respective ER-PM tethering capacities as we described above.

We then wondered if such PLs-binding capacity is conserved. Interestingly, TM-truncated VAPB (VAPBN) could also bind PI, but not PS (Supplementary Fig. 3e). These data may explain the fact that highly expressed VAPB was unable to establish ER-PM contacts near fission yeast cell tips where PS is accumulated [32] (Fig. 3e). PI-VAPBN binding was greatly enhanced by PI_4P, while $PI_{4,5}P_2$ only had a minor effect (Fig. 3d). To obtain physiological implications of PI/PIPs-VAPB interactions, we turned to familial ALS8 mutant $VAPB^{P56S}$ [33] which harbors a single mutation within the VCS (Fig. 1d). $VAPBN^{P56S}$ showed a comparable PI binding affinity as VAPBN, but a clearly weaker PI_4P association, whereas its $PI_{4,5}P_2$ affinity seemed negligible (Supplementary Fig. 3e and Fig. 3d). As expected, $VAPB^{P56S}$ was compromised in ER-PM tethering, both at cell tips and along cell sides (Fig. 3e).

In summary, fission yeast VAPs can interact with major anionic PLs, which requires the MSP domain. Binding of PI and PI_4P is likely a conserved feature of VAP family.

VAP-anionic phospholipids interactions underlie ER-PM tethering mechanism

Given that binding affinity of VAP variants with major anionic PLs was correlative to their ER-PM tethering capacity, we hypothesized that such lipid-protein interactions could be the basis for ER-PM contact formation in fission yeast.

To directly test this idea, we used *pps1Δ* cells lacking the only PS-synthesizing cytidine diphosphate-diacylglycerol (CDP-DAG)-serine O-phosphatidyltransferase in *S. pombe* (Fig. 4a). It has been shown that *pps1Δ* cells have no detectable PS but exhibit an increased PI level [34]. Indeed, as previously shown [32], the PM pool of PS marked by GFP-Lact-C2 [35] was absent in *pps1Δ* (Supplementary Fig. 4a). We also saw augmented PM levels of PI_4P and $PI_{4,5}P_2$ indicated by PH_{Osh2}-GFP and PH_{Num1}-GFP [5] respectively in these cells

(Supplementary Fig. 4a), mirroring overall high PI content. ER-PM contact formation was however unaffected in *pps1Δ* (Fig. 4b and Supplementary Fig. 4b).

In fission yeast, PI synthesis is controlled by the essential gene *pis1* that encodes a CDP-DAG-inositol 3-phosphatidyltransferase [36] (Fig. 4a). Unlike budding yeast, *S. pombe* is a natural inositol auxotroph lacking the *de novo* synthesis pathway (Fig. 4a) [37,38], which allows us to limit levels of PI and/or PIPs via inositol starvation. Although no method has been established to visually indicate PI abundance in yeast, a gradual decline in cellular PI level was observed after inositol starvation [39]. Intriguingly, considerably large PM regions were deprived of the ER in inositol-starved *pps1Δ*, but not in such starved *WT* cells (Fig. 4b; Supplementary Movie 1). Both PM levels of PI_4P and $PI_{4,5}P_2$ were significantly lowered after inositol starvation (Supplementary Fig. 4a). We think that loss of ER-PM contacts specifically seen in inositol-starved *pps1Δ* cells was not due to cell death-related ER mis-organization which also occurred in *WT* after inositol starvation (Supplementary Fig. 4b). It is rather a consequence of lacking major anionic PLs – the PM counterparts of VAP-mediated ER-PM tethering machinery.

As PI_4P and $PI_{4,5}P_2$ are generally scarce in the ER membrane, we further envisaged that ER-PM contacts kept by PM-anchored Scs2 in *scs2Δscs22Δ* backgrounds would be more vulnerable in a shortage of major abundant anionic PLs - PI and PS. Indeed, large ER-free PM regions were readily seen in *scs2Δscs22Δpps1Δ* cells highly expressing Scs2-PM, while these cells mostly lost ER-PM contacts after grown in inositol-free medium, resulting in clustered ER compartments in the cytoplasm (Fig. 4c).

Therefore, we conclude that major anionic PLs, including PI, PS, PI_4P and $PI_{4,5}P_2$, collectively act as the essential PM binding partners underpinning VAP-mediated ER-PM tethering in fission yeast.

VAP-mediated ER-PM contact formation is responsive to cytosolic pH

It has been shown that charge-based interactions of several PH domains with PI_4P and $PI_{4,5}P_2$ are pH-sensitive and abolished at low pH (e.g., pH 6 and pH 6.8 for their *in vitro* binding of PH_{OSBP} respectively) [40]. Our *in vitro* liposome binding results also showed similarly reduced affinities of Scs2N to both PI and PS at a lower pH (pH 5), suggestive of their possible binding through electrostatic attractions (Supplementary Fig. 5a).

We adopted two different approaches to decrease cytosolic pH (pH_c): 1) inactivation of proton-transporting ATPases by energy depletion (ED) (i.e, by inhibiting both glycolysis and mitochondrial electron transport); 2) treatment with semi-permeable sorbic acid (SA) [41,42]. In both cases, pH_c in *WT* dropped below 5.5 within two hours indicated by the genetically encoded pH sensor sfpHluorin [43] (Supplementary Fig. 5b). Interestingly, both PI_4P and $PI_{4,5}P_2$ markers lost the cortical binding after two-hour treatments, while the PS indicator left the cortex only in cells treated with ED but not SA (Fig. 5a). It should be noted that PI_4P and $PI_{4,5}P_2$ markers no longer reflect corresponding lipid levels at low pH_c where charge-based lipid-marker interactions are compromised [40]. On the other hand, lipid markers that bind via non-charge-based interactions, e.g., sterols and diacylglycerol (DAG), are possibly pH-insensitive and indeed remained membrane-associated after cytoplasmic acidification (Supplementary Fig. 5c). Localizational difference of the PS marker after treatments should be unrelated to low pH_c, which also implies a specific role of energy metabolic pathways in maintaining the PM level of PS.

Importantly, ER-PM contacts were significantly reduced in these *WT* cells after both treatments (Fig. 5b; Supplementary Movie 2). Notably, PM affinity of Scs2 was greatly reduced in energy-depleted cells to almost $Scs2^{3KA}$ level within two hours, manifested by decreased cortex-to-NE ratios (Fig. 5c,d). Such affinity reduction occurred progressively as PI_4P, $PI_{4,5}P_2$ and PS markers sequentially lost the PM localization (Fig. 5d). As PI_4P marker

left the cortex immediately upon cell exposure to ED buffer before possible pH_c decline, we favored the idea that these cells lost the PM pool of PI_4P at the early stage with unknown mechanisms. PM affinity of Scs2 did not obviously reduce in SA-treated cells (Fig. 5c), which was not simply due to the presence of PS in the PM (Fig. 5a), as *pps1Δ* lacking PS also exhibited similarly after SA treatment (Supplementary Fig. 5d). We guessed that either PM PI levels or PI-Scs2 interactions could be affected differently in ED- and SA-treated cells. Somewhat as indirect evidence, we found that Pdr16, a presumed PI transporter [44], lost the PM binding only in cells treated with ED but not SA (Supplementary Fig. 5c). In fact, it left the cortex prior to the PS marker in these cells (Fig. 5d), which may reflect reduced PI availability in the PM after energy depletion. We confirmed that fission yeast Pdr16 bound PI *in vitro* (Supplementary Fig. 5e). Concordantly, PM localization of Pdr16 was barely visible in inositol-starved *pps1Δ* cells which should have lost most PI (Supplementary Fig. 5f).

Collectively, these results again demonstrate our view that the cortical binding of Scs2 indeed depends on interactions with major anionic PLs. It further suggests that lipid-protein interaction-based ER-PM contacts are responsive to cytosolic pH.

Scs2 modulates the plasma membrane H+-ATPase Pma1 activity via FFAT-like motif-mediated interaction for pH_c homeostasis

Given that the major pH_c regulator Pma1 was among the top hits of Scs2-interactors (Fig. 2b), we wondered if Scs2 plays a role in pH_c homeostasis. Interestingly, we identified a highly conserved FFAT-like motif within the P domain of Pma1 across fungi (Fig. 6a). Either the removal or genetic alterations of this presumed Scs2-interacting motif engendered inviable spores in *S. pombe* (Fig. 6a), indicative of its necessity for Pma1 function. $Scs2^{3KA}$ lacking the functional MSP domain that is known FFAT motif-associated [22], did exhibit much weaker binding to Pma1 (Supplementary Fig. 6a).

Recently resolved Pma1 structures in both *S. cerevisiae* and *N. crassa* have pinpointed autoinhibitory regulation of Pma1 through intra- or inter-molecular interactions between P and R domains [15,16]. Remarkably, the FFAT-like motif is right at this P-R interface (Fig. 6b), implicating Scs2 in Pma1 regulation. In fact, *scs2Δscs22Δ* cells already showed compromised growth in highly acidic media, similarly to *pma1-ΔCter* cells that lacked the C-terminal R domain (Fig. 6c). Moreover, Scs2 appeared to play a specific role in surviving extreme acid environments, as *pma1-ΔCter* cells became more sensitive to low pH when they further lost Scs2 (Fig. 6c).

Surprisingly, *WT* cells expressing both Scs2-GFP-TM and Pma1-mCherry are sensitive to highly acidic media, similarly to that of Pma1-mCherry-expressing *scs2Δscs22Δ* cells (Fig. 6c). These data suggest that pH-related growth defects associated with *scs2Δ* were not simply due to ER-PM contact loss. Intriguingly, Scs2-Pma1 interaction was totally abolished in these Pma1-mCherry-expressing *WT* cells where Scs2 was GFP-tagged (Fig. 6d). In contrast, such growth defects were not seen in *WT* cells when Scs2 was tagged with 3HA and Scs2-Pma1 interaction was retained (Fig. 6c,d). Thus, Scs2-Pma1 interaction is important for cell survival in acid environments. Besides, Pma1-mCherry localization was unaffected in all these backgrounds regardless of functional VAPs or Scs2-Pma1 interaction (Supplementary Fig. 6b), indicating that Scs2-mediated modulation is non-essential for wild-type Pma1 trafficking to the PM. On the other hand, Pma1-ΔCter-mCherry localized normally to the PM in the presence of Scs2-Pma1 interaction. However, it became defective in the ER exit without this interaction (Supplementary Fig. 6c), implying that Scs2 binding might also aid proper Pma1 assembly or maturation.

We then imagined that Scs2-mediated modulation on Pma1 activity could be crucial for pH_c homeostasis. To directly test this idea, we traced pH_c decline in ED-treated cells over time. As expected, unlike in *WT*, pH_c dropped rapidly below six within one hour in cells

lacking either or both of functional Scs2 and Pma1 R domain (Supplementary Fig. 6d). Of note, in these ED-treated *WT* cells, Scs2-Pma1 interaction remained after mild cytoplasmic acidification (Supplementary Fig. 6e). Collectively, our results suggest that FFAT-mediated interaction enables Scs2 to functionally modulate Pma1 for robust pH_c homeostasis.

Altogether, we conclude that conserved electrostatic interactions between VAPs and anionic phospholipids underlie VAP-mediated ER-PM contact formation and hence determine the pH-sensitive nature of ER-PM contacts in fission yeast. We also hypothesize that Scs2 maintains cytosolic pH through its modulatory interaction with Pma1 (Fig. 6e). All such interactions necessitate the conserved MSP domain.

Discussion

VAP-protein interactions taken place at various MCSs, especially the ones bridged by FFAT motifs, have been widely regarded as primary 'molecular pillars' underlying VAP-mediated membrane tethering [1,2]. Here, we provided both *in vitro* and *in vivo* evidence to postulate an alternative viewpoint that electrostatic VAP-lipid interactions are the major molecular forces at least for ER-PM coupling in fission yeast. Conceivably, major anionic PLs of the PM (comprised of ~ 20% PI, 10% PS and 1% PI_4P + $PI_{4,5}P_2$ in yeast [31,45]) are in much higher abundance than VAPs, which makes the extent of ER-PM contacts dependent on VAP dosage. We believe that such tethering mechanism should not be merely limited to *S. pombe* or to ER-PM contacts, as binding of PI and PI_4P appears to be conserved in VAP family and other organelles may also contain adequate levels of PI and/or PI_4P in cytosolic leaflets [30,46]. Thus, much lower PI content in the mammalian PM as compared to that of yeasts [30,47,48] and non-conserved PS-binding ability of VAPs may partially explain different scales of ER-PM association in these cell types. On the other hand, distribution of PI and PI_4P among

organelles could in turn define preferential sorts of VAP-mediated ER contacts for a given cell type under various conditions.

VAPs facilitate recruitment of several ORP/Osh proteins and subsequently their non-vesicular sterol/PI_4P transfer at ER-PM/Golgi contact sites to allow ER-resident Sac1-mediated PI_4P metabolism and hence sustain PI_4P levels in respective membranes [9,49]. Of interest, our data suggest that the ER localization of VAPs is no longer required for this PI_4P metabolism in fission yeast when VAP-mediated ER-PM contacts are intact. Thus, VAPs likely have no impact on directionality of such lipid transfer at MCSs. It has been speculated that ORP/Osh-dependent sterol/PI_4P countertransport and Sec14 family-mediated PI/PC exchange may be functionally coupled at ER-PM contacts [50]. Here we showed that the cortical localization of Sec14-like Csr102 is fully dependent on VAPs, which somewhat substantiates the possibility of such interconnected lipid exchange cycles via VAPs, although exact functions of Csr102 still await further investigation. Additionally, VAPs' affinity to a wide range of anionic PLs could further make them an ideal regulatory nexus to coordinate multiple lipid exchange reactions at MCSs. It is thus attractive to speculate that ALS-associated $VAPB^{P56S}$ with reduced PI_4P affinity may fail such coordination hence promoting disease progression.

Ionized status of anionic PLs is pH-dependent, thus their electrostatic interactions with proteins are pH-sensitive and mainly prevail at pHs above respective pKa. For instance, as pKa values for the 4-phosphate moiety of PI_4P (~6.3) and $PI_{4,5}P_2$ (~6.7) [51] fall within the physiological range, their interactions with proteins are vulnerable to cytosolic acidification [40]. Similarly, we saw a sequential loss of PM binding for $PI_{4,5}P_2$ and PI_4P markers in SA-treated cells as pH_c decreased (data not shown). However, ionization of PI (pKa ~2.5) and PS (pKa ~5.5) is less likely affected by regular pH_c oscillation [52]. Indeed, protein binding of PI and PS remained when pH_c dropped below 5.5 in SA-treated cells. As discussed, we think that

available PM pools of PI and PS are specifically reduced after energy depletion. Conceivably, ATP consumption that drives lipid conversion and circulation is likely required to maintain PI and PS levels in the PM.

Glucose/energy sensing is intimately linked to Pma1 regulation. It is widely accepted that the C-terminal R domain is autoinhibitory at normal pH_c by immobilizing other cytosolic domains via a clamp-like interaction with the P domain [15,16,53-56]. By releasing the cytosolic domains, phosphorylation of the R domain upon glucose sensing rapidly activates Pma1 [17,57]. Our study suggests a second regulatory module in interfering Pma1 autoinhibition via an FFAT-VAP-mediated competitive binding to the P domain. This module could act to prolong Pma1 activity in cells facing low glucose to avoid rapid cytoplasmic acidification. Ultrastructural insights will help to address if such interactions are constantly stimulative or versatile dependently on conditions. We conceive that such modulatory VAP-Pma1 interaction mainly works *in trans* across ER-PM contacts. However, a certain portion of their *cis* interactions may facilitate Pma1 assembly in the ER and its proper packaging for ER exit, especially when it lacks the R domain. It remains to be seen if VAPs play such a general role in protein trafficking, considering they interact widely with vesicle trafficking machinery.

Of note, PS has been shown enriched in the PM regions surrounding transmembrane proteins, including that of Pma1 [31]. A recent study also found that several TMs of Pma1 exhibted a preferred binding with PS in the inner PM leaflet [16]. It is thus likely that PS binding of Scs2 may facilitate its access to the vicinity of Pma1 for the modulatory interaction. Another enthralling idea is that pH_c-sensory interactions of Scs2 with PI_4P and $PI_{4,5}P_2$ might autonomously signal its favored binding towards Pma1 when pH_c drops. We therefore hypothesize that VAPs balance pH_c by gearing preferential interactions between Pma1 and pH-biosensory PLs at ER-PM contacts. Since both interactions appear conserved, this strategy could be widely shared by other organisms.

Methods

Experimental Model and Subject Details

All fission yeast strains used in this study are listed in Supplementary Table 1. Strains were constructed from laboratory stocks using standard methods. The artificial ER-PM tether (TM-GFP/mCherry-CSS_{Ist2}) and the control construct (TM-GFP/mCherry) established previously in [5] were expressed from *leu1* locus under Thiamine-repressible *nmt1* promoter. The PI_4P marker PH_{Osh2}-mCherry was designed as PH_{Osh2}-GFP previously reported in [5] and was constitutively expressed from *ura4* locus under *rtn1* promoter. The PS marker GFP-Lact-C2 [35] was expressed from *ade6* locus under *act1* promoter, the sterol marker GFP-D4H [57] was expressed from *leu1* locus under *pil1* promoter, and the DAG maker C1δ-GFP amplified from rat PKCδ C1-containing plasmid (Addgene #21216) [59] was expressed from *ura4* locus under *scs2* promoter. The pH sensor superfolder pHluorin (sfpHluorin) amplified from p426MET25-sfpHluorin (Addgene #115697) [43] were expressed from *leu1* locus under *pil1* promoter.

The strain where *scs2* and *scs22* swapped their genomic loci shown in Supplementary Fig. 1a was made by replacing the entire open reading frame of one gene with the other (inclusive of introns for both genes). Scs2-3HA-TM and Scs22-3HA-TM were generated by inserting three tandem HA epitopes between S360 and P361 of Scs2 or between I296 and H297 of Scs22 that expressed from their respective native locus under their own promoters, in the same way as previously described [5]. Scs2-mCherry-PM or $Scs2^{3KA}$-mCherry-PM was generated by inserting mCherry after S360 and by replacing TM region with the PM targeting motif (“KKKKKKSKTKCVIM”) from human K-Ras4B [29]. It was expressed from *leu1* locus under either *nmt1* or *pil1* promoter. VAPB-GFP-TM or $VAPB^{P56S}$-GFP-TM was generated by inserting GFP between P213 and R214 of VAPB or $VAPB^{P56S}$ that expressed from *leu1*

locus under *pil1* promoter. GFP-tagged Scs2 and Scs22 were expressed from respective native locus unless otherwise stated. In *scs2Δscs22Δ* background, as annotated in Fig. 1-2 and Supplementary Fig. 1-3, GFP-tagged Scs2 and Scs22 were expressed from *leu1* locus under *scs2* or *pil1* promoter, and GFP-tagged mutants and swop variants (i.e., $Scs2^{3KA}$ or $Scs2^{K36/38/43A}$, $Scs22^{3KA}$ or $Scs22^{K36/38/43A}$, $MSP_{scs2(1-125)}$-LK-$TM_{scs22(122-319)}$, and $MSP_{scs22(1-121)}$-LK-$TM_{scs2(126-383)}$) were expressed from *leu1* locus under *pil1* promoter. C-terminally GFP tagged N-terminus (lacking only the TM domain) of either Scs2 (i.e., Scs2N or $Scs2N^{1-360}$) or Scs22 (i.e., Scs22N or $Scs22N^{1-296}$) used for proteomics analyses in Fig. 2 and Supplementary Fig. 2 was expressed from respective native locus. C-terminally GFP tagged N-terminus of VAP variants (namely Scs2N, Scs22N, $Scs2N^{3KA}$, $Scs22N^{3KA}$, $VAPBN^{1-213}$ and $VAPBN^{1-213(P56S)}$) used for liposome analyses in Fig. 3 and Supplementary Fig. 3,5 were expressed from *leu1* locus under *pil1* promoter in *scs2Δscs22Δ* cells.

C-terminally tagged Csr102 or Pdr16 were expressed from their respective native locus. C-terminally 3HA or mCherry tagged Pma1 mutants were all expressed from the native locus. Mutations located in the FFAT-like motif of Pma1 resulted in spontaneous diploidization. Pma1-ΔFFAT was made by a deletion of 13 amino acids from 591P to 603D; Pma1-4L was made by substituting all 594E, 597D, 600E and 603D with leucine; Pma1-$FFAT_{Opi1}$ was constructed by replacing 10 amino acids from 594E to 603D by "DDEEFFDASE" from budding yeast Opi1. $Pma1^{\Delta Cter}$ was generated by deleting its last 23 amino acids (897Q-919A).

For all experiments unless otherwise stated, *S. pombe* cells were grown exponentially at 24 °C in YES (yeast extract with supplements) or EMMS (Edinburgh minimal media supplemented with appropriate amino acids) before specific treatments or imaging. *pps1Δ* cells were freshly grown on YES medium plate supplemented with 0.4 mM ethanolamine (Merck, 398136-25ML) before liquid culture. Expression of artificial constructs under *nmt1*

promoter was induced in EMMS for at least 20 hours. EMMS with 5 mg/mL thiamine (Thi) (Sigma-Aldrich, T1270-25G) was used to suppress the construct expression. For inositol starvation experiments, cells were cultured in EMMS without inositol for at least 21 hours.

Microscopy

Scanning confocal microscopy was performed on an Olympus FLUOVIEW FV3000 (Olympus Corporation, Japan) equipped with a U Plan Super Apochromat 100X, 1.4 NA Oil immersion objective lens, a 488 nm (for GFP excitation) and a 561 nm (for mCherry excitation) solid state laser, with high sensitivity-spectral detectors. Typically, we acquired image stacks that consisted of 21 z-sections with 0.24 µm spacing or 9 z-sections with 0.5 µm spacing (55.2 nm per pixel).

We also employed Nikon TiE system (CFI Plan Apochromat VC 100X, 1.4 N.A. objective) equipped with Yokogawa CSU-X1-A1 spinning disk unit, the Photometrics CoolSNAP HQ2 (129 nm per pixel with 2 × 2 binning) or Prime 95B™ Scientific CMOS camera (110 nm per pixel) and a DPSS 405 nm 100 mW, a DPSS 491 nm 100 mW and DPSS 561 nm 50 mW laser illumination under the control of MetaMorph Premier Ver. 7.7.5 to collect single or multiple z-plane images or to perform fluorescence recovery after photobleaching (FRAP) experiments. Typically, a 10 × 10 pixels circular region at the cell cortex (top plane) was bleached with a sequence of 200 high-intensity laser iterations and then subsequent images were taken every 0.5 second for 25 seconds or 1 minute for 5 minutes.

Unless otherwise stated, imaging was performed on *S. pombe* cells placed in sealed growth chambers containing 2% agarose YES medium or indicated growth medium. Only interphase cells were used in all image analysis in this paper.

Proteomics for VAPs, protein level estimation and Co-immunoprecipitation (Co-IP)

Cells expressing Scs2N$^{1-360}$-GFP, Scs2-GFP-TM, Scs22N$^{1-296}$-GFP, Scs22-GFP-TM or GFP control were grown to log phase, harvested with freshly prepared buffer A (50 mM Tris-HCl, 150 mM NaCl, 2 mM EDTA, 1% Nonidet P (NP)-40, 50 mM NaF, 0.1 mM Na_3VO_4, 1 mM PMSF, 1.5 mM Benzamidine-HCl, and Roche protease inhibitor cocktail). Cells were mixed with glass beads and homogenized in a Mini Bead Beater (Biospec, OK, USA) at 4 °C and total cell lysates were harvested after removing cell debris. Lysates were adjusted to the same total protein concentration using buffer B (10 mM Tris-HCl, 150 mM NaCl, 0.5 mM EDTA, 50 mM NaF, 0.1 mM Na_3VO_4, pH 7.4, added with protease inhibitors) before incubation with GFP-Trap beads (Chromotek, Munich, Germany) for one hour at 4 °C. Beads were washed with buffer B and resuspended in SDS loading buffer. Co-immunoprecipitated proteins were visualized with Coomassie staining reagent (Bio-Rad), and excised gel segments were sent for LC-MS/MS analysis. All mass spectrometry was performed by Protein and Proteomics Center (PPC) in the National University of Singapore.

For protein level estimation in Fig. 1b,3e and Supplementary Fig. 1d, total cell lysates were harvested as described above, and then subjected SDS-PAGE and western blotting probed by rabbit anti-GFP (Abcam, MA, USA) and mouse anti-α-tubulin antibodies (TAT-1, a gift from K. Gull, University of Oxford, UK). For detection, IRDye800 conjugated anti-mouse and IRDye680 conjugated anti-rabbit antibodies were used and subsequent quantification analyses were done on the Odyssey infrared imaging system (LI-COR, NE, USA) and ImageJ 1.48v software package (NIH, MD, USA).

For co-immunoprecipitation, glass bead-homogenized cells or cryo-ground (only for Co-IP experiments with Pil1-mGFP) were suspended in 300 µL of buffer A at 4 ^{o}C and total cell lysates were harvested after removing cell debris. We used low salt buffers where NaCl concentration was 50 mM for Co-IP experiments with Pil1-mGFP and Pma1-mCherry.

Typically, lysates were adjusted to the same total protein concentration, diluted with buffer C (the same recipe as buffer A but without NP-40) and precleared for non-specific binding by incubation with Dynabeads™ Protein G (Invitrogen, CA, USA) for one hour at 4 ^{o}C. The pre-cleared lysate was then subjected to incubation with rabbit anti-GFP, rabbit anti-mCherry (Abcam, MA, USA), or mouse anti-HA (Roche, Basel, Switzerland) antibody for one hour at 4 ^{o}C and then with Dynabeads™ Protein G for 45 minutes at 4 ^{o}C. Beads were washed five times with buffer C and additionally one time with 1% NP-40-containing buffer A. We also repeated experiments shown in Fig. 6d and Supplementary Fig. 6a,e with ChromoTek RFP-Trap magnetic beads (Proteintech, IL, USA). Samples were resuspended in SDS-loading buffer and subjected SDS-PAGE and western blotting probed by rabbit anti-GFP, rabbit anti-mCherry or mouse anti-HA antibodies.

Recombinant protein purification

Scs2N-6His-expressing plasmid-containing BL21 (DE3) cells were cultured in Lysogenia Broth (LB) medium at 37°C to an OD_{600} of 0.7-1.0. Protein expression was then induced by 0.5 mM IPTG for 5-6 hours or overnight at 24°C. Cells were lysed by sonication in buffer D (50 mM NaH_2PO_4 (pH 8), 500 mM NaCl, 40 mM Imidazole, 2 mM PMSF, 0.001 g/mL lysozyme) and debris were removed by centrifugation at 20,000 g for 15 mins at 4°C. Scs2N-6His was purified using the standard protocol with the Thermo Scientific™ HisPur™ Ni-NTA spin column.

Liposome preparation

Lipids were purchased from either Sigma-Aldrich: L-α-phosphatidylcholine (PC, egg yolk) or Avanti Polar Lipids: L-α-phosphatidylinositol (PI, soy); L-α-phosphatidylserine (PS, brain); L-α-phosphatidylinositol-4-phosphate (PI_4P, brain); L-α-phosphatidylinositol-4,5-

biphosphate ($PI_{4,5}P_2$, brain); and 1,2-dioleoyl-sn-glycero-3-phosphoethanolamine-N-(lissamine rhodamine B sulfonyl) (Rhod-PE). Lipids were dissolved and mixed in chloroform and dried using SpeedVac vacuum concentrator (Eppendorf, HH, DE) for 24 hours.

For co-sedimentation assays, respective lipid films (i.e., 100% PC (mol/mol); 75% PC and 25% PI; 20% PC and 80% PI; 75% PC and 25% PS; 20% PC and 80% PS; 73% PC, 25% PI and 2% PI_4P; 73% PC, 25% PS and 2% PI_4P) were hydrated with buffer E (20 mM HEPES, 25 mM NaCl, 0.75 M sucrose, pH 7) and sonicated for 20 mins at 65°C. Liposomes were passed through polycarbonate membrane with a pore size of 100 nm using the MiniExtruder (Avanti Polar Lipids, AL, USA) at 65°C. Liposomes were washed with buffer F (20 mM HEPES, 25 mM NaCl, pH 7) and concentrated by centrifugation at 32,000 g for 30 mins at 4°C.

For binding assays, respective 1% Rhod-PE containing lipid films (i.e., 99% PC; 74% PC and 25% PI; 74% PC and 25% PS; 72% PC, 25% PI and 2% PI_4P; 72% PC, 25% PI and 2% $PI_{4,5}P_2$; 72% PC, 25% PS and 2% PI_4P; 72% PC, 25% PS and 2% $PI_{4,5}P_2$) were hydrated with buffer F or G (the same recipe as buffer F but with a pH of 5) and sonicated for 20 mins at 65°C. Aggregates were removed by centrifugation at 21,100 g for 30 mins at 4°C. Liposome concentration was normalized by the rhodamine intensity of 2.5% NP-40-lysed liposomes using the Spark multimode microplate reader (Tecan, Männedorf, Switzerland).

Liposome co-sedimentation assay

Purified Scs2N-6His was incubated with respective liposomes for 30 mins at 4°C with gentle agitation. The mixture was pelleted by centrifugation at 32,000 g for 30 mins at 4°C. Both the supernatant and pellet (after washing with buffer F) were resuspended with SDS-loading buffer for SDS-PAGE and western blotting probed by mouse anti-His antibody (Abcam, MA, USA).

Liposome binding assay

Normalized soluble lysates of *scs2Δscs22Δ* cells expressing either Scs2N-GFP, Scs2N^{3KA}-GFP, VAPBN-GFP or VAPBN^{P56S}-GFP were freshly prepared using buffer C (with 50 mM NaCl) and incubated with rabbit anti-GFP antibody for one hour and then with Dynabeads™ Protein G for one hour at 4°C with gentle agitation. Dynabeads conjugated with protein of interest were washed with buffer C before incubation with normalized Rhod-PE-containing liposomes for one hour at 4°C. Soluble *scs2Δscs22Δ* cell lysate was used as the negative control. liposomes were prepared with buffer G for assays preformed under pH 5. Dynabeads were harshly washed with buffer F or G and imaged by confocal microscope on 96-well plates.

Energy depletion and sorbic acid treatment

Freshly washed cells were incubated on rotary shaker with 1 mL 8mM sorbic acid/EMM or energy depletion buffer (EMM without glucose, 20 mM 2-geoxyglucose (2-DG), 10 µM antimycin A) before imaging. For confocal imaging, cells were placed on an agarose pad prepared from respective media.

Cytosolic pH measurement

Cytosolic pH of sfpHluorin-expressing cells after various treatments was indicated from fluorescence intensities obtained by confocal microscopy using DAPI/GFP (Excitation: 405 nm; Emission: 488 nm) and GFP/GFP (Excitation and emission: 488 nm) filter sets as previously described [41]. DAPI/GFP to GFP/GFP intensity (simplified as 405/488) ratios were used to designate the cytosolic pH against the standard calibration curve. To generate the calibration curve, sfpHluorin-expressing cells were treated with calibration buffers (50 mM

MES, 50 mM HEPES, 50 mM KCl, 50 mM NaCl, 0.2 M ammonium acetate, 75 mM monensin, 10 mM nigericin, 10 mM 2-DG and 10 mM NaN_3) of various pH (5.15, 5.51, 6.03. 6.65, 7.17, and 7.73 in Supplementary Fig. 5b; 5.0, 5.5, 6.0. 6.5, 7.0, and 7.5 in Supplementary Fig. 6d). As previously described [60], calibration buffers allowed rapid equilibration of the intracellular and extracellular pH. The standard curve was made by plotting 405/488 ratios of these cells under each pH condition against respective pH.

pH sensitivity growth assay

Cells were firstly cultured in YES till exponential growth phase. ~0.05 OD_{595} of fresh cells were used for each growth assay performed on the 24-well plate: cells were grown in YES of respective pH (2.5, 3.2, and 4) at 30 °C (1.5 mL per well). OD_{595} was measured by the Spark multimode microplate reader every 6 hours for 12 hours.

Image processing

Intensity profile analysis

For intensity profile analysis shown in Fig. 3b, we selected a non-medial region (avoiding the nucleus) using a line of 40-pixel width perpendicular to the long cell axis at central focal plane of a cell and obtained initial intensity the profile of PH_{Osh2}-GFP using “Plot Profile” built-in plugin in ImageJ. Intensity corrected by background subtraction was normalized respectively as $\hat{I}F = IF/IF_{Max}$, where IF_{Max} represents the maximum corrected intensity along the line. Normalized intensity and positional information were replotted using MATLAB with a moving average (n=2). Only interphase cells were used for the analysis.

3D rendering

For 3D renderings shown in Fig. 5b and Supplementary Movies 1,2, z-stack images were taken with 0.24 µm spacing on Olympus FLUOVIEW FV3000. Image deconvolution was performed using adaptive point spread function module in Autoquant (Media Cybernetics, Bethesda, MD). 3D rendering was carried out using Imaris software module (Bitplane, South Windsor, CT, USA).

Quantification and statistical Analysis

Measurement of cortex/NE ratio of VAP variants

For each analyzed cell, regions of the cortical ER and the nuclear envelope (NE) were manually outlined according to the localization of either GFP (in Fig. 1c,e) or mCherry-tagged (in Fig. 5d) VAP variants or the ER luminal marker mCherry-ADEL (in Fig. 1c,e) at the central focal plane. Mean intensities of respective regions were measured by ImageJ and corrected by background subtraction. The ratio between corrected intensities of corresponding regions was defined as cortex/NE ratio. In particular, cortex/NE ratios of VAP variants shown in Fig. 1c,e were normalized by dividing corresponding cortex/NE ratios of mCherry-ADEL of the same cell. Only interphase cells were used for the analysis.

FRAP analysis

Average fluorescence intensity of the bleached region was corrected for both the background and non-specific bleaching that based on the intensity of a non-bleached cell in the same filed. Corrected intensity for each time point was normalized as $\hat{I}F(t) = [IF(t) - IF(0)]/[IF(-\Delta t) - IF(0)]$, where $IF(-\Delta t)$ represents intensity before photobleaching and $IF(0)$ is the first intensity following bleaching. Normalized recovery curves were fitted with a simple single exponential function $IF(t)=F(1-e^{-kt})$ in MATLAB. Recovery half time was calculated as $\ln(2)/k$ for Supplementary Fig. 1b,c,2i.

Proteome-wide FFAT scoring

A sequence unit of every continuous 13 residues mimicking a FFAT-like motif (i.e., six flank residues preceding seven core amino acids) was used for scoring based on the position weight matrix as previously described [4,23]. For each given protein, the FFAT score shown in Fig. 2b,c,6a and Supplementary Fig. 2a,d was the minimal score obtained by scanning over the entire protein sequence. The scoring system was coded in Python and available upon request.

Liposome binding analysis

Calculation of relative liposome binding

We measured mean GFP and Rhodamine intensities for each analyzed Dynabeads using ImageJ as $F_{protein}$ and $F_{liposome}$ respectively. For each liposome type (25% PI or 25% PS), average values of $F_{protein}$ and $F_{liposome}$ from all beads incubated with control lysates (i.e. $\overline{F}^{control}_{protein}$ and $\overline{F}^{control}_{liposome}$) were used for correction, and relative liposome binding of the tested protein for each bead was calculated as $(F^{WT/3KA}_{liposome} - \overline{F}^{control}_{liposome})/(F^{WT/3KA}_{protein} - \overline{F}^{control}_{protein})$ or 0 (if $F^{WT/3KA}_{liposome} < \overline{F}^{control}_{liposome}$) shown with box plots in Fig. 3c. Pseudo-colored images were all with the same contrast for each fluorescent channel. We set the highest rhodamine intensity obtained from the binding assay of the corresponding VAP mutant with 99% PC liposomes as the binding threshold, which is marked by a dotted line and shadow shown in Fig. 3d and Supplementary Fig. 3c,e,5e.

Calculation of liposome binding coefficient κ_b

Pairs of raw intensities $F_{protein}$ and $F_{liposome}$ were fitted with $F_{liposome} = \kappa_b F_{protein} + \varepsilon$ to obtain κ_b and the corresponding r^2 in MATLAB for each liposome type shown in Fig. 3d and

Supplementary Fig. 3d. We only compared κ_b calculated from the same experiment where liposome amounts used can be equalized as described above.

κ_b calculation and image correction under pH 5

GFP and Rhodamine intensities altered significantly due to pH shift, we thus did intensity correction for a rational κ_b comparison between different pH conditions. We assumed that 1) κ_b of Scs2N-GFP for 99% PC liposomes remained unaffected from pH 7 to pH 5; 2) a linear intensity transformation from pH 7 to pH 5 could apply to both GFP and Rhodamine by introducing simplified correction factors δ_G and δ_R respectively. Raw intensity data for 99% PC were fitted with $\delta_R F_{liposome}^{pH5} = \kappa_b^{pH5} \delta_G F_{protein}^{pH5} + \varepsilon'$ and $F_{liposome}^{pH7} = \kappa_b^{pH7} F_{protein}^{pH7} + \varepsilon$ to get δ_G and δ_R, which were used to calculate κ_b^{pH5} for other liposome type shown in Supplementary Fig. 5a. Original images for pH 5 were correspondingly corrected by δ_G or δ_R using ImageJ built-in function "Multiply…".

Protein structure modeling

S. pombe Pma1 structure (E108-D918) shown in Fig. 6b was modeled using the SWISS-MODEL web server with *S. cerevisiae* Pma1 (7vh5.1.A) [15] as the template. Shown intramolecular and intermolecular interactions between the R domain and the FFAT-like motif were predicted according to the autoinhibited structure of *N. crassa* Pma1 (7ny1.1.C) [16].

Statistical evaluation

Statistical tests, sample size and definition of error bars and measured values were provided either in figures or figure legends. *P*-values and r^2 were computed using MATLAB ttest2() function and 'Curve Fitting Toolbox' respectively. Pearson correlation coefficients

(Pearson's r) in Fig. 2a were calculated in Excel. Cophenetic distances shown in Fig. 2a,6a were calculated from hierarchical clustering using MATLAB and Vector NTI respectively.

References

1 Wu, H., Carvalho, P. & Voeltz, G. K. Here, there, and everywhere: The importance of ER membrane contact sites. *Science* **361**, doi:10.1126/science.aan5835 (2018).

2 Eisenberg-Bord, M., Shai, N., Schuldiner, M. & Bohnert, M. A Tether Is a Tether Is a Tether: Tethering at Membrane Contact Sites. *Dev Cell* **39**, 395-409, doi:10.1016/j.devcel.2016.10.022 (2016).

3 Loewen, C. J., Roy, A. & Levine, T. P. A conserved ER targeting motif in three families of lipid binding proteins and in Opi1p binds VAP. *EMBO J* **22**, 2025-2035, doi:10.1093/emboj/cdg201 (2003).

4 Slee, J. A. & Levine, T. P. Systematic prediction of FFAT motifs across eukaryote proteomes identifies nucleolar and eisosome proteins with the predicted capacity to form bridges to the endoplasmic reticulum. *Contact (Thousand Oaks)* **2**, 1-21, doi:10.1177/2515256419883136 (2019).

5 Zhang, D., Vjestica, A. & Oliferenko, S. Plasma membrane tethering of the cortical ER necessitates its finely reticulated architecture. *Curr Biol* **22**, 2048-2052, doi:10.1016/j.cub.2012.08.047 (2012).

6 Manford, A. G., Stefan, C. J., Yuan, H. L., Macgurn, J. A. & Emr, S. D. ER-to-plasma membrane tethering proteins regulate cell signaling and ER morphology. *Dev Cell* **23**, 1129-1140, doi:10.1016/j.devcel.2012.11.004 (2012).

7 Schulz, T. A. & Creutz, C. E. The tricalbin C2 domains: lipid-binding properties of a novel, synaptotagmin-like yeast protein family. *Biochemistry* **43**, 3987-3995, doi:10.1021/bi036082w (2004).

8 Fischer, M. A., Temmerman, K., Ercan, E., Nickel, W. & Seedorf, M. Binding of plasma membrane lipids recruits the yeast integral membrane protein Ist2 to the cortical ER. *Traffic* **10**, 1084-1097, doi:10.1111/j.1600-0854.2009.00926.x (2009).

9 Stefan, C. J. *et al.* Osh proteins regulate phosphoinositide metabolism at ER-plasma membrane contact sites. *Cell* **144**, 389-401, doi:10.1016/j.cell.2010.12.034 (2011).

10 Zhang, D., Bidone, T. C. & Vavylonis, D. ER-PM Contacts Define Actomyosin Kinetics for Proper Contractile Ring Assembly. *Curr Biol* **26**, 647-653, doi:10.1016/j.cub.2015.12.070 (2016).

11 Zhang, D. Interplay between endoplasmic reticulum membrane contacts and actomyosin cytoskeleton. *Cytoskeleton (Hoboken)* **77**, 241-248, doi:10.1002/cm.21623 (2020).

12 Ng, A. Y. E., Ng, A. Q. E. & Zhang, D. ER-PM Contacts Restrict Exocytic Sites for Polarized Morphogenesis. *Curr Biol* **28**, 146-153 e145, doi:10.1016/j.cub.2017.11.055 (2018).

13 Holsbeeks, I., Lagatie, O., Van Nuland, A., Van de Velde, S. & Thevelein, J. M. The eukaryotic plasma membrane as a nutrient-sensing device. *Trends Biochem Sci* **29**, 556-564, doi:10.1016/j.tibs.2004.08.010 (2004).

14 Auer, M., Scarborough, G. A. & Kuhlbrandt, W. Three-dimensional map of the plasma membrane H+-ATPase in the open conformation. *Nature* **392**, 840-843, doi:10.1038/33967 (1998).

15 Zhao, P. *et al.* Structure and activation mechanism of the hexameric plasma membrane H(+)-ATPase. *Nat Commun* **12**, 6439, doi:10.1038/s41467-021-26782-y (2021).
16 Heit, S. *et al.* Structure of the hexameric fungal plasma membrane proton pump in its autoinhibited state. *Sci Adv* **7**, eabj5255, doi:10.1126/sciadv.abj5255 (2021).
17 Lecchi, S. *et al.* Tandem phosphorylation of Ser-911 and Thr-912 at the C terminus of yeast plasma membrane H+-ATPase leads to glucose-dependent activation. *J Biol Chem* **282**, 35471-35481, doi:10.1074/jbc.M706094200 (2007).
18 Kabeche, R., Baldissard, S., Hammond, J., Howard, L. & Moseley, J. B. The filament-forming protein Pil1 assembles linear eisosomes in fission yeast. *Mol Biol Cell* **22**, 4059-4067, doi:10.1091/mbc.E11-07-0605 (2011).
19 Loewen, C. J. & Levine, T. P. A highly conserved binding site in vesicle-associated membrane protein-associated protein (VAP) for the FFAT motif of lipid-binding proteins. *J Biol Chem* **280**, 14097-14104, doi:10.1074/jbc.M500147200 (2005).
20 Zhang, D., Vjestica, A. & Oliferenko, S. The cortical ER network limits the permissive zone for actomyosin ring assembly. *Curr Biol* **20**, 1029-1034, doi:10.1016/j.cub.2010.04.017 (2010).
21 Ng, A. Q. E., Ng, A. Y. E. & Zhang, D. Plasma Membrane Furrows Control Plasticity of ER-PM Contacts. *Cell Rep* **30**, 1434-1446 e1437, doi:10.1016/j.celrep.2019.12.098 (2020).
22 Kaiser, S. E. *et al.* Structural basis of FFAT motif-mediated ER targeting. *Structure* **13**, 1035-1045, doi:10.1016/j.str.2005.04.010 (2005).
23 Murphy, S. E. & Levine, T. P. VAP, a Versatile Access Point for the Endoplasmic Reticulum: Review and analysis of FFAT-like motifs in the VAPome. *Biochim Biophys Acta* **1861**, 952-961, doi:10.1016/j.bbalip.2016.02.009 (2016).
24 Nakase, Y., Nakamura, T., Okazaki, K., Hirata, A. & Shimoda, C. The Sec14 family glycerophospholipid-transfer protein is required for structural integrity of the spindle pole body during meiosis in fission yeast. *Genes Cells* **9**, 1275-1286, doi:10.1111/j.1365-2443.2004.00806.x (2004).
25 Phillips, S. E. *et al.* Yeast Sec14p deficient in phosphatidylinositol transfer activity is functional in vivo. *Mol Cell* **4**, 187-197, doi:10.1016/s1097-2765(00)80366-4 (1999).
26 Lee, W. L., Bezanilla, M. & Pollard, T. D. Fission yeast myosin-I, Myo1p, stimulates actin assembly by Arp2/3 complex and shares functions with WASp. *J Cell Biol* **151**, 789-800, doi:10.1083/jcb.151.4.789 (2000).
27 Thayer, N. H. *et al.* Identification of long-lived proteins retained in cells undergoing repeated asymmetric divisions. *Proc Natl Acad Sci U S A* **111**, 14019-14026, doi:10.1073/pnas.1416079111 (2014).
28 Ercan, E. *et al.* A conserved, lipid-mediated sorting mechanism of yeast Ist2 and mammalian STIM proteins to the peripheral ER. *Traffic* **10**, 1802-1818, doi:10.1111/j.1600-0854.2009.00995.x (2009).
29 Choy, E. *et al.* Endomembrane trafficking of ras: the CAAX motif targets proteins to the ER and Golgi. *Cell* **98**, 69-80, doi:10.1016/S0092-8674(00)80607-8 (1999).
30 van Meer, G., Voelker, D. R. & Feigenson, G. W. Membrane lipids: where they are and how they behave. *Nat Rev Mol Cell Biol* **9**, 112-124, doi:10.1038/nrm2330 (2008).
31 van 't Klooster, J. S. *et al.* Periprotein lipidomes of Saccharomyces cerevisiae provide a flexible environment for conformational changes of membrane proteins. *Elife* **9**, doi:10.7554/eLife.57003 (2020).

32 Haupt, A. & Minc, N. Gradients of phosphatidylserine contribute to plasma membrane charge localization and cell polarity in fission yeast. *Mol Biol Cell* **28**, 210-220, doi:10.1091/mbc.E16-06-0353 (2017).
33 Nishimura, A. L. *et al.* A mutation in the vesicle-trafficking protein VAPB causes late-onset spinal muscular atrophy and amyotrophic lateral sclerosis. *Am J Hum Genet* **75**, 822-831, doi:10.1086/425287 (2004).
34 Matsuo, Y., Fisher, E., Patton-Vogt, J. & Marcus, S. Functional characterization of the fission yeast phosphatidylserine synthase gene, pps1, reveals novel cellular functions for phosphatidylserine. *Eukaryot Cell* **6**, 2092-2101, doi:10.1128/EC.00300-07 (2007).
35 Yeung, T. *et al.* Membrane phosphatidylserine regulates surface charge and protein localization. *Science* **319**, 210-213, doi:10.1126/science.1152066 (2008).
36 Gaynor, P. M. & Greenberg, M. L. Regulation of CDP-diacylglycerol synthesis and utilization by inositol and choline in Schizosaccharomyces pombe. *J Bacteriol* **174**, 5711-5718, doi:10.1128/jb.174.17.5711-5718.1992 (1992).
37 Ridgway, G. J. & Douglas, H. C. Unbalanced growth of yeast due to inositol deficiency. *J Bacteriol* **76**, 163-166, doi:10.1128/jb.76.2.163-166.1958 (1958).
38 Henry, S. A., Klig, L. S. & Loewy, B. S. The genetic regulation and coordination of biosynthetic pathways in yeast: amino acid and phospholipid synthesis. *Annu Rev Genet* **18**, 207-231, doi:10.1146/annurev.ge.18.120184.001231 (1984).
39 Fernandez, S., Homann, M. J., Henry, S. A. & Carman, G. M. Metabolism of the phospholipid precursor inositol and its relationship to growth and viability in the natural auxotroph Schizosaccharomyces pombe. *J Bacteriol* **166**, 779-786, doi:10.1128/jb.166.3.779-786.1986 (1986).
40 Shin, J. J. H. *et al.* pH Biosensing by PI4P Regulates Cargo Sorting at the TGN. *Dev Cell* **52**, 461-476 e464, doi:10.1016/j.devcel.2019.12.010 (2020).
41 Munder, M. C. *et al.* A pH-driven transition of the cytoplasm from a fluid- to a solid-like state promotes entry into dormancy. *Elife* **5**, doi:10.7554/eLife.09347 (2016).
42 Orij, R., Postmus, J., Ter Beek, A., Brul, S. & Smits, G. J. In vivo measurement of cytosolic and mitochondrial pH using a pH-sensitive GFP derivative in Saccharomyces cerevisiae reveals a relation between intracellular pH and growth. *Microbiology (Reading)* **155**, 268-278, doi:10.1099/mic.0.022038-0 (2009).
43 Reifenrath, M. & Boles, E. A superfolder variant of pH-sensitive pHluorin for in vivo pH measurements in the endoplasmic reticulum. *Sci Rep* **8**, 11985, doi:10.1038/s41598-018-30367-z (2018).
44 Stastny, D. *et al.* Yeast Sec14-like lipid transfer proteins Pdr16 and Pdr17 bind and transfer the ergosterol precursor lanosterol in addition to phosphatidylinositol. *FEBS Lett*, doi:10.1002/1873-3468.14558 (2022).
45 McLaughlin, S. & Murray, D. Plasma membrane phosphoinositide organization by protein electrostatics. *Nature* **438**, 605-611, doi:10.1038/nature04398 (2005).
46 Drin, G. MapPIng PI inside cells brings new light to polyphosphoinositide biology. *J Cell Biol* **219**, doi:10.1083/jcb.202001185 (2020).
47 Pemberton, J. G. *et al.* Defining the subcellular distribution and metabolic channeling of phosphatidylinositol. *J Cell Biol* **219**, doi:10.1083/jcb.201906130 (2020).
48 Zewe, J. P. *et al.* Probing the subcellular distribution of phosphatidylinositol reveals a surprising lack at the plasma membrane. *J Cell Biol* **219**, doi:10.1083/jcb.201906127 (2020).
49 Mesmin, B. *et al.* A four-step cycle driven by PI(4)P hydrolysis directs sterol/PI(4)P exchange by the ER-Golgi tether OSBP. *Cell* **155**, 830-843, doi:10.1016/j.cell.2013.09.056 (2013).

50 Helle, S. C. *et al.* Organization and function of membrane contact sites. *Biochim Biophys Acta* **1833**, 2526-2541, doi:10.1016/j.bbamcr.2013.01.028 (2013).
51 van Paridon, P. A., de Kruijff, B., Ouwerkerk, R. & Wirtz, K. W. Polyphosphoinositides undergo charge neutralization in the physiological pH range: a 31P-NMR study. *Biochim Biophys Acta* **877**, 216-219, doi:10.1016/0005-2760(86)90137-2 (1986).
52 Marsh, D. Handbook of lipid bilayers. CRC Press. (1990)
53 Kuhlbrandt, W., Zeelen, J. & Dietrich, J. Structure, mechanism, and regulation of the Neurospora plasma membrane H+-ATPase. *Science* **297**, 1692-1696, doi:10.1126/science.1072574 (2002).
54 Hippe, S. & Luth, H. A simple physical model for fungicide induced hexagonal clustering of intramembrane particles in the plasmalemma of Ustilago avenae. *J Theor Biol* **121**, 351-366, doi:10.1016/s0022-5193(86)80114-x (1986).
55 Portillo, F. & Serrano, R. Growth control strength and active site of yeast plasma membrane ATPase studied by site-directed mutagenesis. *Eur J Biochem* **186**, 501-507, doi:10.1111/j.1432-1033.1989.tb15235.x (1989).
56 Palmgren, M. G., Sommarin, M., Serrano, R. & Larsson, C. Identification of an autoinhibitory domain in the C-terminal region of the plant plasma membrane H(+)-ATPase. *J Biol Chem* **266**, 20470-20475 (1991).
57 Lecchi, S., Allen, K. E., Pardo, J. P., Mason, A. B. & Slayman, C. W. Conformational changes of yeast plasma membrane H(+)-ATPase during activation by glucose: role of threonine-912 in the carboxy-terminal tail. *Biochemistry* **44**, 16624-16632, doi:10.1021/bi051555f (2005).
58 Maekawa, M. Domain 4 (D4) of Perfringolysin O to Visualize Cholesterol in Cellular Membranes-The Update. *Sensors (Basel)* **17**, doi:10.3390/s17030504 (2017).
59 Codazzi, F., Teruel, M. N. & Meyer, T. Control of astrocyte Ca(2+) oscillations and waves by oscillating translocation and activation of protein kinase C. *Curr Biol* **11**, 1089-1097, doi:10.1016/s0960-9822(01)00326-8 (2001).
60 Brett, C. L., Tukaye, D. N., Mukherjee, S. & Rao, R. The yeast endosomal Na+K+/H+ exchanger Nhx1 regulates cellular pH to control vesicle trafficking. *Mol Biol Cell* **16**, 1396-1405, doi:10.1091/mbc.e04-11-0999 (2005).

Acknowledgments

We thank Dr. Yasunori Saheki for sharing the original plasmid to construct GFP-D4H in this study. We are grateful to Dr. Gregory Jedd for sharing human cDNA and protein purification protocol. Authors were funded by the Temasek Life Sciences Laboratory.

Author Contributions

D.Z. conceived and supervised the project. K.L.H. and D.Z. established liposome assays. K.L.H. and T.S. did protein purification and western blots. B.M. did pH sensitivity tests. B.M., T.S. and K.L.H. performed drug treatment and measured cytosolic pH. B.M., T.S.,

A.Y.E.N., and A.Q.E.N. did Co-IP experiments. T.S., B.M., K.L.H., A.Y.E.N., and D.Z. performed confocal microscopy. B.M., T.S. and A.Y.E.N. did FRAP analyses. K.L.H., B.M., T.S, D.Z., A.Y.E.N., and A.Q.E.N. constructed strains. D.Z. did interatom, bioinformatics and other quantitative analyses. D.Z. wrote the paper. K.L.H. and B.M. contributed to the manuscript.

Competing interests

Authors declare no competing interests.

Materials & Correspondence

This study did not generate new unique reagents. Plasmids generated in this study are available upon request. Further information and requests for resources and reagents should be directed to and will be fulfilled by Dan Zhang (zhangdan@tll.org.sg).

Figure legends

Figure 1

Fission yeast VAPs mediate ER-PM contact formation through the conserved MSP domain in a dosage dependent manner. (**a**,**c**,**e**) Spinning disk confocal images of indicated cells expressing indicated proteins. Shown are central focal planes. Yellow arrowheads point to cell tips lacking ER-PM contacts. Normalized cortex/NE ratios (mean±standard deviation [SD]) of fission yeast VAP variants are included. *p*-values, two-tailed t test, ***$p<10^{-7}$<**$p<0.0001$; n.s., not significant. n, cell number. Scale bars, 5 μm. (**b**) Expression levels of GFP-tagged VAP variants in indicated cells. Relative ratios of protein levels as compared to Scs2 level (asterisked) in wild type (*WT*) are included. Protein samples were probed with anti-GFP and anti–α-Tubulin antibodies. (**d**) The cartoon shows the design of VAP swop

variants, and the alignment of consensus sequences from fission yeast VAPs and human VAPB. TM, the C-terminal transmembrane domain. Blue asterisks show mutated sites in this work and the magenta asterisk indicates the ALS-associated VAPB mutation.

Figure 2

Interactome analyses implicate VAPs in functional modulation of Sec14 family and predict a non-protein-protein interaction-based ER-PM tethering mechanism for VAPs. (**a**) A statistical overview of interactome results summarized from Supplementary Data 1. Numbers of overlapped interactors are included in the Venn diagram. Scale bar, cophenetic distance. (**b**) Co-IP of indicated proteins expressed from native loci. Samples were probed with indicated antibodies. The top five hits of Scs2 interactors localizing to the lateral cell cortex are shown in the table. (**c**) Sec14-like lipid transporters detected in interactome analyses are shown with numbers of detected peptides and the corresponding minimal FFAT scores. (**d-g**) Scanning confocal images of indicated cells expressing indicated proteins. Shown are central focal planes. Scs2, Scs2-GFP-TM; ER, the luminal marker GFP-ADEL. Pma1, Pma1-mCherry. Scale bars, 5 μm.

Figure 3

Conserved binding of VAPs with major anionic phospholipids underlies the membrane tethering function. (**a,b**) Scanning confocal images of indicated cells expressing indicated proteins. Shown are central focal planes. The cartoon in (**a**) shows the design of the PM-anchored mCherry-tagged Scs2 variants. In (**b**), intensity profiles of PH_{Osh2}-GFP over illustrated regions of analyzed cells were shown in the bottom. Thi, thiamine. n, cell number. (**c,d**) Fluorescence microscopy-based protein-liposome binding assays. Indicated GFP-tagged VAP variants immobilized on Dynabeads were incubated with indicated rhodamine-labelled

liposomes (see Methods for details). In (**c**), shown are pseudo-colored spinning disk confocal images with the same contrast for each fluorescent channel. Quantifications are shown on the right. Plots from raw intensity data are included in (**d**); the dotted line and shadow mark the liposome binding threshold. *p*-values, two-tailed t test, ***$p<10^{-5}$; κ_b, liposome binding coefficient; r^2, r squared; n, bead number. (**e**) Central focal plane scanning confocal images of indicated cells. Yellow arrowheads point to the cortical regions lacking ER-PM contacts. Expression levels of GFP-tagged Scs2 and VAPB variants are shown on the right. Scale bars, 5 μm.

Figure 4

VAP-mediated ER-PM contact formation is compromised in cells lacking inositol and PS. (**a**) Pathways for PI and PS synthesis in fission yeast. *De novo* inositol biosynthesis pathway in *S. cerevisiae* that absent in *S. pombe* is shown in grey. (**b,c**) Scanning confocal images of indicated cells expressing indicated proteins cultured in the presence or absence of inositol. Red arrowheads designate the cytoplasmic ER compartments. Yellow arrowheads point to the cortical regions lacking ER-PM contacts. EMMS, Edinburgh minimal media supplemented with appropriate amino acids. Scale bars, 5 μm.

Figure 5

VAP-mediated ER-PM contact formation compromised in cells with low cytosolic pH. (**a**) Scanning confocal images of *WT* cells expressing various phospholipid markers after indicated treatments. Shown are central focal planes. (**b**) Scanning confocal images of *WT* cells expressing mCherry-ADEL after various treatments. The corresponding 3D-rendered cortical snapshots of asterisked cells are shown in the bottom. (**c**) Spinning disk confocal images of *WT* cells expressing Scs2-GFP-TM after indicated treatments. (**d**) Reduction in

cortex/NE ratios of Scs2-mCherry-TM after energy depletion in *WT* cells. Shown are representative central focal plane spinning disk confocal images of indicated cells with or without the treatment. Time, relative to buffer shift. Cortex/NE ratios of Scs2-GFP-TM and Scs2^{3KA}-GFP-TM from non-treated cells are included as controls. Time windows for the initiation of each indicated events are highlighted with corresponding colors. Error bars represent 2×SD. n, cell number. Scale bars, 5 μm.

Figure 6

Scs2 modulates Pma1 activity via FFAT-like motif-mediated interaction for pH$_c$ homeostasis. (**a**) Predicted FFAT-like motif locating within the P domain of Pma1 is highly conserved in Fungi and essential for Pma1function in fission yeast. *S.p, S. pombe; S.c, S. cerevisiae; E.g, E. gossypii; K.l, K. lactis; C.g, C. glabrata; M.o, M. oryzae; N.c, N. crassa; C.a, C. albicans*. The underlined Opi1 sequence is the part replacing the corresponding Pma1 segment in *pma1-FFAT$_{Opi1}$* mutant. Black asterisks mark mutated residues and red asterisks point to colonies or inviable spores carrying indicated pma1 mutants. (**b**) Predicted structure of fission yeast Pma1 monomer (108E-918D). TM (transmembrane), A (actuator), N (nucleotide-binding), P (phosphorylation), and R (regulatory) domains are indicated. Contact between R domain and FFAT-like motif is illustrated in the frame. Predicted intramolecular (R-P) and intermolecular (R-P'of the adjacent monomer) interactions during R domain-mediated autoinhibition are shown with dotted lines. Involved residues are conserved between *S. pombe* and *N. crassa*. S911 and T912 are conserved phosphorylation sites for autoinhibitory regulation. (**c**) Growth assays of indicated cells in medium with different pH. Relative growth (OD_{12hr}/OD_{0hr}) over 12 hours is indicated by both number and color. pH-sensitive strains were highlighted in red. (**d**) Co-IP of indicated proteins expressed from native loci. Samples were probed with indicated antibodies. (**e**) A model for mechanisms of

VAP-mediated ER-PM contact formation and yeast VAP function in pH_c homeostasis via Pma1 modulation. M, MSP domain.

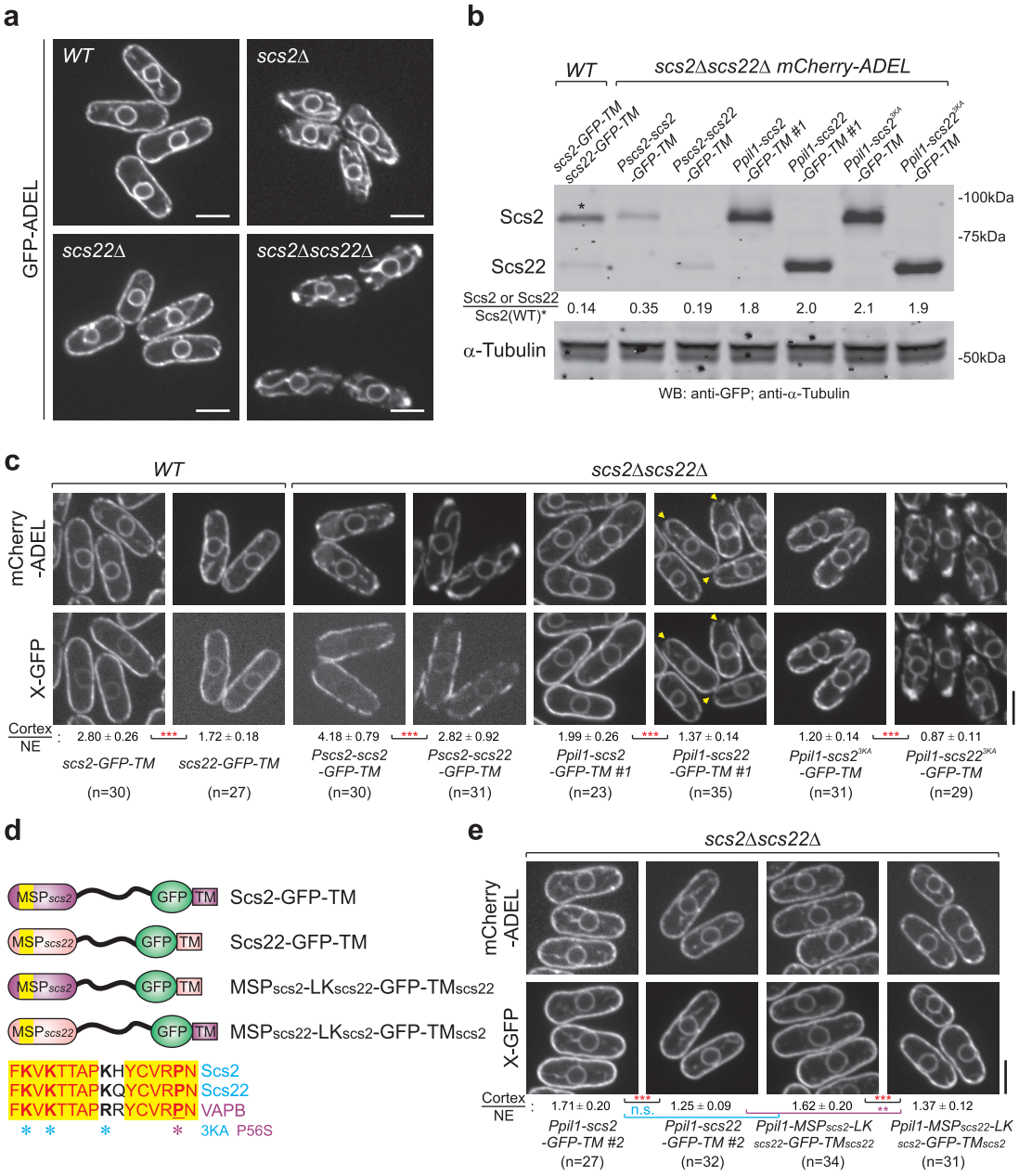
a
GFP-ADEL
WT
scs2Δ
scs22Δ
scs2Δscs22Δ
b
WT
scs2Δscs22Δ mCherry-ADEL
scs2-GFP-TM
scs22-GFP-TM
Pscs2-scs2 -GFP-TM
Pscs2-scs22 -GFP-TM
Ppil1-scs2 -GFP-TM #1
Ppil1-scs22 -GFP-TM #1
Ppil1-scs2^3KA -GFP-TM
Ppil1-scs22^3KA -GFP-TM
Scs2
Scs22
-100kDa
-75kDa
Scs2 or Scs22 / Scs2(WT)*
0.14 0.35 0.19 1.8 2.0 2.1 1.9
α-Tubulin
-50kDa
WB: anti-GFP; anti-α-Tubulin
c
WT
scs2Δscs22Δ
mCherry -ADEL
X-GFP
Cortex / NE :
2.80 ± 0.26 *** 1.72 ± 0.18
scs2-GFP-TM (n=30) scs22-GFP-TM (n=27)
4.18 ± 0.79 *** 2.82 ± 0.92
Pscs2-scs2 -GFP-TM (n=30) Pscs2-scs22 -GFP-TM (n=31)
1.99 ± 0.26 *** 1.37 ± 0.14
Ppil1-scs2 -GFP-TM #1 (n=23) Ppil1-scs22 -GFP-TM #1 (n=35)
1.20 ± 0.14 *** 0.87 ± 0.11
Ppil1-scs2^3KA -GFP-TM (n=31) Ppil1-scs22^3KA -GFP-TM (n=29)
d
MSPscs2 GFP TM Scs2-GFP-TM
MSPscs22 GFP TM Scs22-GFP-TM
MSPscs2 GFP TM MSPscs2-LKscs22-GFP-TMscs22
MSPscs22 GFP TM MSPscs22-LKscs2-GFP-TMscs2
FKVKTTAPKHYCVRPN Scs2
FKVKTTAPKQYCVRPN Scs22
FKVKTTAPRRYCVRPN VAPB
* * * * 3KA P56S
e
scs2Δscs22Δ
mCherry -ADEL
X-GFP
Cortex / NE :
1.71 ± 0.20 *** n.s. 1.25 ± 0.09
1.62 ± 0.20 *** ** 1.37 ± 0.12
Ppil1-scs2 -GFP-TM #2 (n=27)
Ppil1-scs22 -GFP-TM #2 (n=32)
Ppil1-MSPscs2-LK scs22-GFP-TMscs22 (n=34)
Ppil1-MSPscs22-LK scs2-GFP-TMscs2 (n=31)

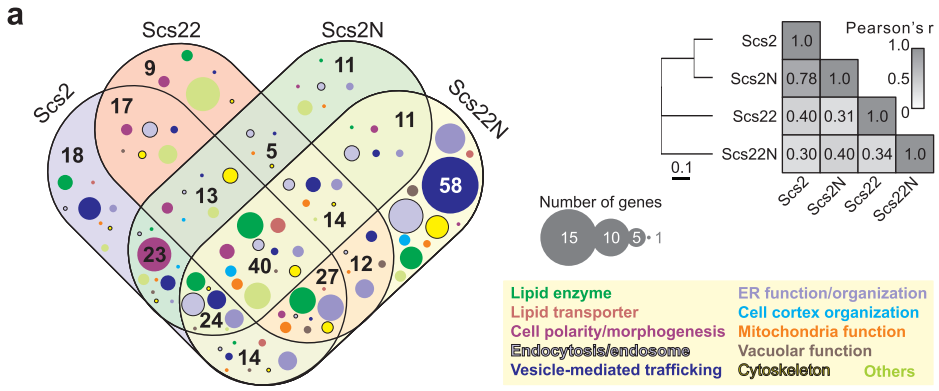

b

# of detected peptides

Gene	Scs2	Scs22	Scs2N	Scs22N	FFAT Score
pdr16	85	5	53	20	3.5
csr102	63	32	8	49	4.2
pma1	51	14	17	78	2.5
pil1	24	10	9	18	5
myo1	42	0	20	48	4.5

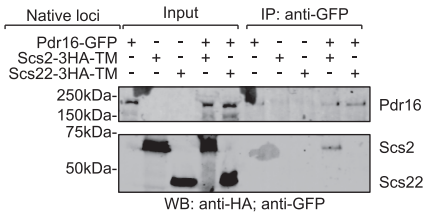

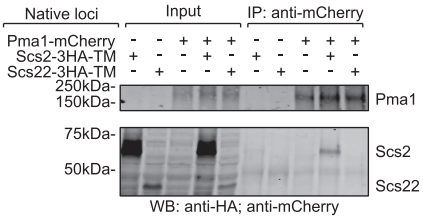

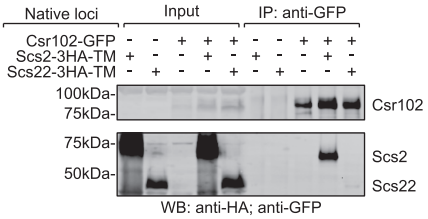

c

Sec14-like Lipid Transporters

Gene	Scs2	Scs22	Scs2N	Scs22N	FFAT Score
pdr16	85	5	53	20	3.5
csr102	63	32	8	49	4.2
csr103	6	5	0	14	3.5
sec14	4	0	0	17	5

# of detected peptides

e

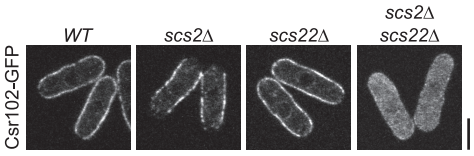

d

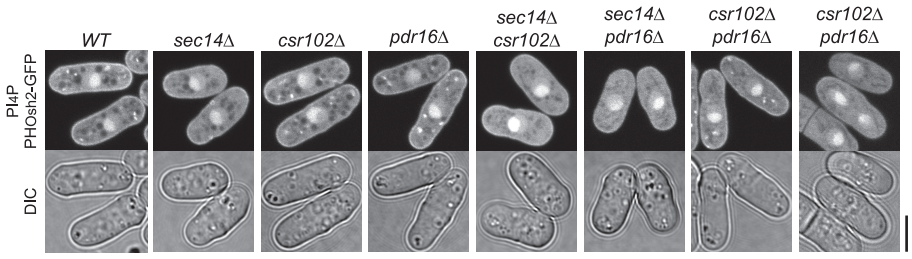

f

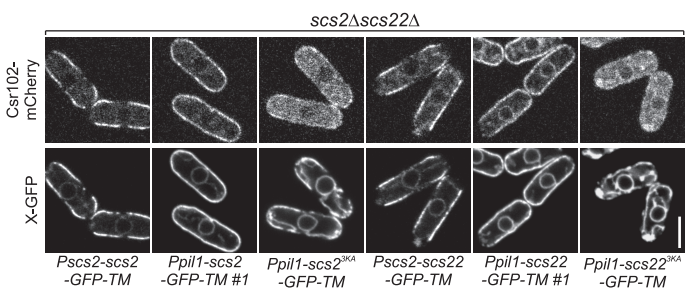

g

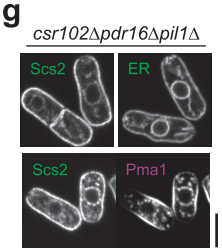

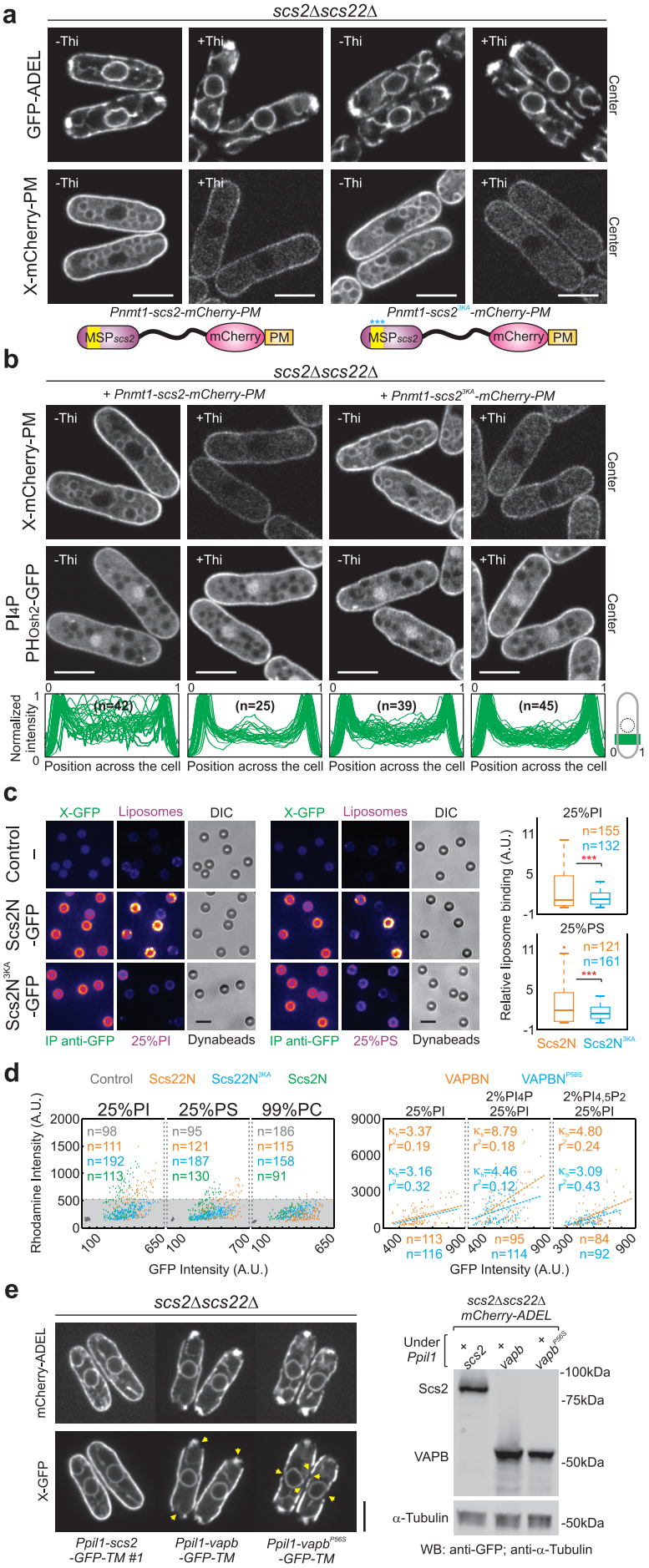
a
scs2Δscs22Δ
GFP-ADEL
X-mCherry-PM
-Thi
+Thi
Center
Pnmt1-scs2-mCherry-PM
Pnmt1-scs2^3KA-mCherry-PM
MSPscs2
mCherry
PM
b
scs2Δscs22Δ
+ Pnmt1-scs2-mCherry-PM
+ Pnmt1-scs2^3KA-mCherry-PM
X-mCherry-PM
PI4P PHOsh2-GFP
Normalized intensity
(n=42)
(n=25)
(n=39)
(n=45)
Position across the cell
c
X-GFP
Liposomes
DIC
Control
Scs2N -GFP
Scs2N^3KA -GFP
IP anti-GFP
25%PI
Dynabeads
25%PS
Relative liposome binding (A.U.)
n=155
n=132
n=121
n=161
Scs2N
Scs2N^3KA
d
Control
Scs22N
Scs22N^3KA
Scs2N
VAPBN
VAPBN^P56S
25%PI
25%PS
99%PC
2%PI4P 25%PI
2%PI4,5P2 25%PI
Rhodamine Intensity (A.U.)
GFP Intensity (A.U.)
n=98
n=111
n=192
n=113
n=95
n=121
n=187
n=130
n=186
n=115
n=158
n=91
κb=3.37
r²=0.19
κb=3.16
r²=0.32
κb=8.79
r²=0.18
κb=4.46
r²=0.12
κb=4.80
r²=0.24
κb=3.09
r²=0.43
n=113
n=116
n=95
n=114
n=84
n=92
e
scs2Δscs22Δ
mCherry-ADEL
X-GFP
Ppil1-scs2 -GFP-TM #1
Ppil1-vapb -GFP-TM
Ppil1-vapb^P56S -GFP-TM
scs2Δscs22Δ mCherry-ADEL
Under Ppil1
scs2
vapb
vapb^P56S
Scs2
VAPB
α-Tubulin
-100kDa
-75kDa
-50kDa
-50kDa
WB: anti-GFP; anti-α-Tubulin

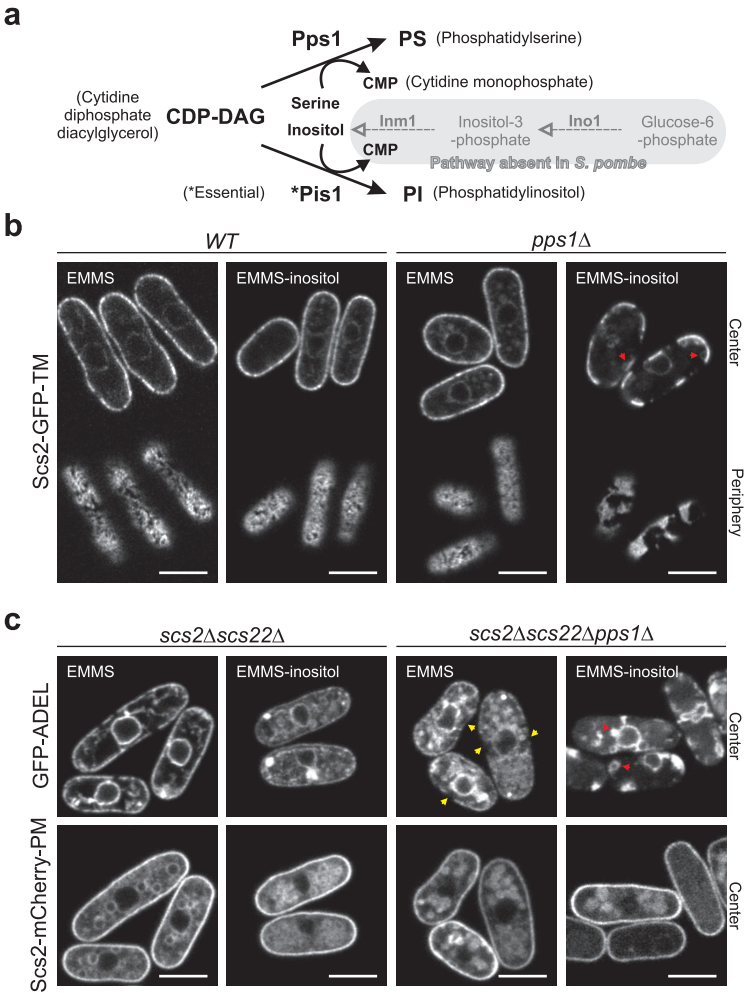
a
Pps1
PS (Phosphatidylserine)
CMP (Cytidine monophosphate)
(Cytidine diphosphate diacylglycerol)
CDP-DAG
Serine
Inositol
CMP
Inm1
Inositol-3 -phosphate
Ino1
Glucose-6 -phosphate
Pathway absent in S. pombe
(*Essential)
*Pis1
PI (Phosphatidylinositol)
b
WT
pps1Δ
EMMS
EMMS-inositol
EMMS
EMMS-inositol
Scs2-GFP-TM
Center
Periphery
c
scs2Δscs22Δ
scs2Δscs22Δpps1Δ
EMMS
EMMS-inositol
EMMS
EMMS-inositol
GFP-ADEL
Center
Scs2-mCherry-PM
Center

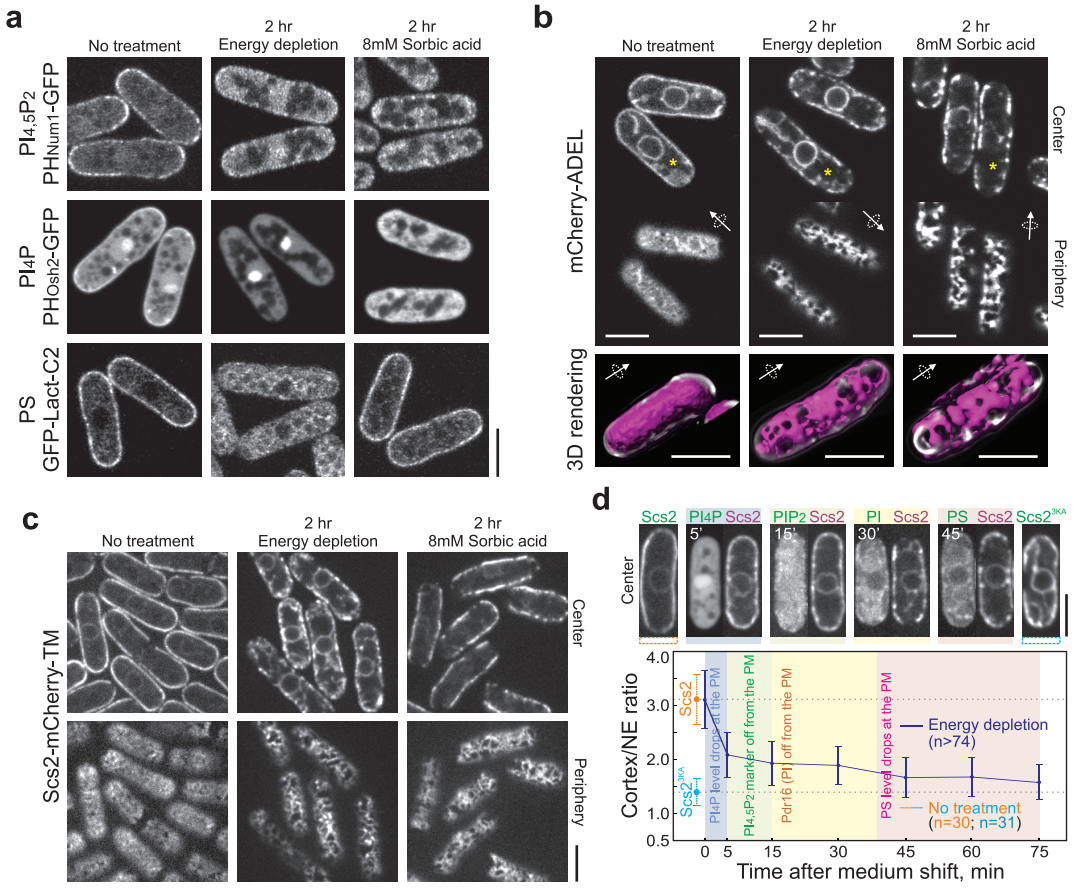
a
No treatment
2 hr Energy depletion
2 hr 8mM Sorbic acid
PI4,5P2 PHNum1-GFP
PI4P PHOsh2-GFP
PS GFP-Lact-C2
b
No treatment
2 hr Energy depletion
2 hr 8mM Sorbic acid
mCherry-ADEL
3D rendering
Center
Periphery
c
No treatment
2 hr Energy depletion
2 hr 8mM Sorbic acid
Scs2-mCherry-TM
Center
Periphery
d
Scs2
PI4P Scs2
PIP2 Scs2
PI Scs2
PS Scs2
Scs2^3KA
5'
15'
30'
45'
Center
Cortex/NE ratio
Scs2
Scs2^3KA
PI4P level drops at the PM
PI4,5P2 marker off from the PM
Pdr16 (PI) off from the PM
PS level drops at the PM
Energy depletion (n>74)
No treatment (n=30; n=31)
Time after medium shift, min

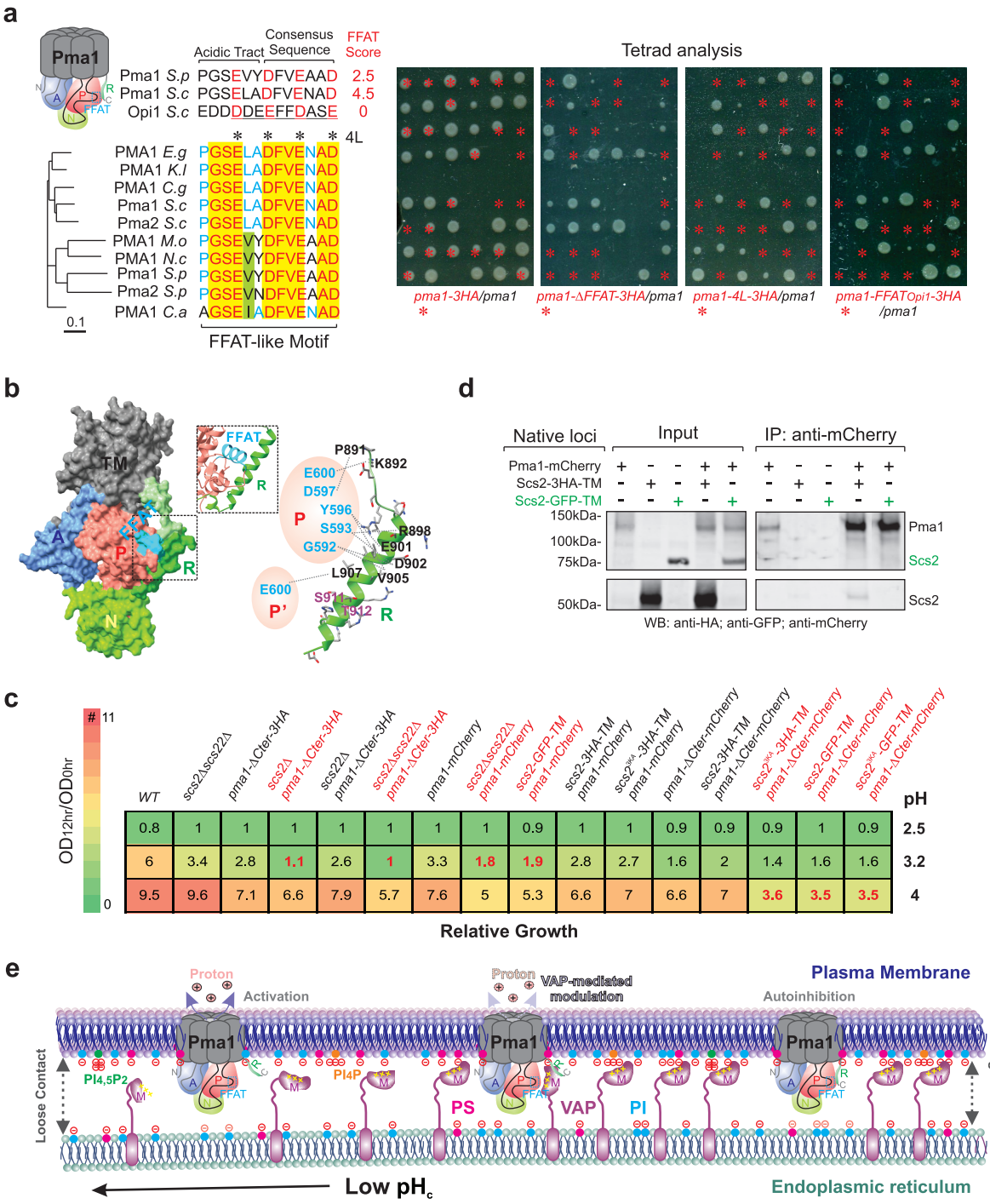
a
Pma1
Acidic Tract
Consensus Sequence
FFAT Score
Pma1 S.p PGSEVYDFVEAAD 2.5
Pma1 S.c PGSELADFVENAD 4.5
Opi1 S.c EDDDDEEFFDASE 0
4L
PMA1 E.g PGSELADFVENAD
PMA1 K.l PGSELADFVENAD
PMA1 C.g PGSELADFVENAD
Pma1 S.c PGSELADFVENAD
Pma2 S.c PGSELADFVENAD
PMA1 M.o PGSEVYDFVEAAD
PMA1 N.c PGSEVYDFVEAAD
Pma1 S.p PGSEVYDFVEAAD
Pma2 S.p PGSEVNDFVEAAD
PMA1 C.a AGSEILADFVENAD
0.1
FFAT-like Motif
Tetrad analysis
pma1-3HA/pma1
pma1-ΔFFAT-3HA/pma1
pma1-4L-3HA/pma1
pma1-FFATOpi1-3HA /pma1
b
TM
A
P
R
N
FFAT
P891
K892
E600
D597
Y596
S593
G592
R898
E901
D902
V905
L907
E600
P'
S911
I912
d
Native loci
Input
IP: anti-mCherry
Pma1-mCherry
Scs2-3HA-TM
Scs2-GFP-TM
150kDa-
100kDa-
75kDa-
50kDa-
Pma1
Scs2
Scs2
WB: anti-HA; anti-GFP; anti-mCherry
c
OD12hr/OD0hr
11
0
WT
scs2Δscs22Δ
pma1-ΔCter-3HA
scs2Δ pma1-ΔCter-3HA
scs22Δ pma1-ΔCter-3HA
scs2Δscs22Δ pma1-ΔCter-3HA
pma1-mCherry
scs2Δscs22Δ pma1-mCherry
scs2-GFP-TM pma1-mCherry
scs2-3HA-TM pma1-mCherry
scs2-3KA-3HA-TM pma1-mCherry
pma1-ΔCter-mCherry
scs2-3HA-TM pma1-ΔCter-mCherry
scs2-3KA-3HA-TM pma1-ΔCter-mCherry
scs2-GFP-TM pma1-ΔCter-mCherry
scs2-3KA-GFP-TM pma1-ΔCter-mCherry
pH
0.8 1 1 1 1 1 1 1 0.9 1 1 0.9 0.9 0.9 1 0.9 2.5
6 3.4 2.8 1.1 2.6 1 3.3 1.8 1.9 2.8 2.7 1.6 2 1.4 1.6 1.6 3.2
9.5 9.6 7.1 6.6 7.9 5.7 7.6 5 5.3 6.6 7 6.6 7 3.6 3.5 3.5 4
Relative Growth
e
Proton
Activation
Proton
VAP-mediated modulation
Plasma Membrane
Autoinhibition
Pma1
PI4,5P2
PI4P
PS
VAP
PI
Loose Contact
Tight Contact
Low pHc
Endoplasmic reticulum